

New Generation Hyperspectral Sensors DESIIS and PRISMA Provide Improved Agricultural Crop Classifications

Itiya Aneece and Prasad S. Thenkabail

Abstract

Using new remote sensing technology to study agricultural crops will support advances in food and water security. The recently launched, new generation spaceborne hyperspectral sensors, German DLR Earth Sensing Imaging Spectrometer (DESIIS) and Italian PRecursores IperSpettrale della Missione Applicativa (PRISMA), provide unprecedented data in hundreds of narrow spectral bands for the study of the Earth. Therefore, our overarching goal in this study was to use these data to explore advances that can be made in agricultural research. We selected PRISMA and DESIIS images during the 2020 growing season in California's Central Valley to study seven major crops. PRISMA and DESIIS images were highly correlated (R^2 of 0.9–0.95). Out of the 235 DESIIS bands (400–1000 nm) and 238 PRISMA bands (400–2500 nm), 26 (11%) and 45 (19%) bands, respectively, were optimal to study agricultural crops. These optimal bands provided crop type classification accuracies of 83–90%. Hyperspectral vegetation indices to estimate plant pigment content, stress, biomass, moisture, and cellulose/lignin content were also identified.

Introduction

Twenty-first century remote sensing calls for increased use of data from hyperspectral sensors to advance the study of agricultural crop characteristics. In the past, this advance has been hindered by the lack of availability of spaceborne hyperspectral data covering the planet. The Hyperion Earth Observing-1 (EO-1) sensor was the first spaceborne hyperspectral sensor with publicly available data that provided significant insights into the possibilities of great scientific advances in the study of agricultural crops and vegetation (Bannari *et al.* 2015; Bhojaraja *et al.* 2015; Breunig *et al.* 2011; Houborg *et al.* 2016; Lamparelli *et al.* 2012; Moharana and Dutta 2016; Pan *et al.* 2013; Sonmez and Slater 2016; Thenkabail *et al.* 2013). EO-1 acquired over 70 000 images of the Earth from the year 2001 through 2015 in 242 narrow spectral bands in the 400–2500 nm spectral range (Aneece and Thenkabail 2018). This acquisition was a quantum leap in spectral data relative to multispectral broadband data acquired in a few broad bands such as from Landsat, Moderate Resolution Imaging Spectroradiometer (MODIS), *Satellite pour l'Observation de la Terre* (SPOT), and the *Indian Remote Sensing* (IRS) series of satellites (Mariotto *et al.* 2013; Marshall and Thenkabail 2015). However, the recent launch of advanced spaceborne hyperspectral sensors such as the Italian PRecursores IperSpettrale della Missione Applicativa (PRISMA) and the German Deutsches Zentrum für Luft- und Raumfahrt (DLR) Earth Sensing Imaging Spectrometer (DESIIS) onboard the International Space Station (ISS) has opened up a new dimension in remote sensing by offering hundreds of hyperspectral narrowbands (HNB) along the electromagnetic spectrum (Heiden *et al.* 2019; Loizzo *et al.* 2016; Lu *et al.* 2020). PRISMA acquires data from 400 to 2500 nm and DESIIS from 400 to 1000 nm (Table 1) and both acquire data

as near-continuous HNB, generating a “spectral signature” rather than a few “data points” as acquired by broadband sensors (Heiden *et al.* 2019; Loizzo *et al.* 2016). In addition, a number of spaceborne hyperspectral sensors were recently launched, such as Germany's Environmental Mapping and Analysis Program (EnMAP) (EnMAP 2022), or planned for launch in the coming years, such as the United States' National Aeronautics and Space Administration (NASA) Surface Biology and Geology (SBG) mission (SBG 2022).

Table 1. Characteristics of hyperspectral data used in this study: Deutsches Zentrum für Luft- und Raumfahrt (DLR) Earth Sensing Imaging Spectrometer (DESIIS) and PRecursores IperSpettrale della Missione Applicativa (PRISMA) (Heiden *et al.* 2019; Loizzo *et al.* 2016).

	DESIIS	PRISMA
Sensor Type	Spaceborne, on ISS	Spaceborne, polar-orbiting
Spectral Range	400 to 1000 nm	400 to 2500 nm
Number of Bands	235	238
Spectral Resolution	2.55 nm	≤12 nm
Spatial Resolution	30 m	30 m; 5 m for panchromatic band
Signal to Noise Ratio (@ 550 nm)	205	200
Radiometric Resolution	13-bit	12-bit
Swath Width	30 km	30 km

ISS = International Space Station.

DESIIS Hyperspectral Data

The German Aerospace Center (formerly DLR) partnered with Teledyne Brown Engineering to design the DLR Earth Sensing Imaging Spectrometer (DESIIS) (Heiden *et al.* 2019; Krutz *et al.* 2019; Peschel *et al.* 2018). It is mounted on the Multi-User System for Earth Sensing (MUSES) platform on the International Space Station (ISS) (Heiden *et al.* 2019). Since the sensor is mounted on the ISS, its coverage depends on the overpasses of the ISS which has a non-sun-synchronous and varied orbit, with no repeat cycle (Heiden *et al.* 2019). Despite the challenges of the variable orbit and collection environments, the cost-savings of mounting DESIIS on the ISS are substantial (Krutz *et al.* 2019). Since it is unable to point at the sun, moon, or deep space for calibration, DESIIS has in-orbit spectral calibration and in-orbit radiometric calibration (Krutz *et al.* 2019). Because of the push broom mechanism, DESIIS data are affected by a low smile effect of 1.7 pixels and an even lower keystone effect of 0.3 pixel across the entire field of view and spectral range (Krutz *et al.* 2019). For details on smile, keystone, striping, and rolling shutter corrections, refer to Alonso *et al.* (2019).

DESIIS has 235 bands along a spectral range from 400 nm to 1000 nm (Heiden *et al.* 2019; Krutz *et al.* 2019). It has a spectral resolution of

US Geological Survey, Western Geographic Science Center, 2255 N. Gemini Rd., Flagstaff, AZ 86001 (ianeece@usgs.gov).

Contributed by Ahmed Abd El-Latif, February 5, 2022 (sent for review May 23, 2022; reviewed by Michael J. Campbell, Xun Geng).

Photogrammetric Engineering & Remote Sensing
Vol. 88, No. 11, November 2022, pp. 715–729.
0099-1112/22/715–729

© 2022 American Society for Photogrammetry
and Remote Sensing
doi: 10.14358/PERS.22-00039R2

2.55 nm with Full Width Half Maximum of approximately 3.5 nm, and a radiometric resolution of 13 bits (Alonso *et al.* 2019; Heiden *et al.* 2019). Its spatial resolution is 30 m, with a 30 km swath at 400 km altitude (Heiden *et al.* 2019). The signal to noise ratio (SNR) varies by band, but at 550 nm the SNR is 205 without binning and 406 at 4 bin (Heiden *et al.* 2019).

DESIS data are now available through Teledyne, in several levels of processing (Heiden *et al.* 2019). The Level 0 product consists of raw data (Heiden *et al.* 2019). The Level 1A product consists of tiled images, a browse image, metadata, and quality flags (Heiden *et al.* 2019). The Level 1B product consists of top of atmosphere (TOA) radiance, with systematic and radiometric corrections including those for the rolling shutter and the smile effect (Heiden *et al.* 2019). The Level 1C product has orthorectified, georeferenced TOA data (Heiden *et al.* 2019). Finally, the Level 2A (L2A) data are atmospherically corrected to ground surface reflectance, available with and without terrain correction (Heiden *et al.* 2019). Atmospheric correction is conducted using the DLR's Python Atmospheric Correction algorithm, based on the Atmospheric and Topographic Correction algorithm (Alonso *et al.* 2019). The L2A data include masks for water, land, cloud, shadow, snow, haze, aerosol optical thickness, and water vapor (Alonso *et al.* 2019). Products are available in four spectral binning configurations: x1, x2, x3, and x4, resulting in the spectral resolutions of 2.55 nm, 5.1 nm, 7.65 nm, and 10.2 nm, respectively (Alonso *et al.* 2019).

PRISMA Hyperspectral Data

The Italian Space Agency's (ASI) *PR*ecursore *I*perSpettrale della *M*issione *A*pplicativa (PRISMA) satellite was launched in 2019 and is in sun-synchronous low-Earth orbit at an altitude of 615 to 620 km (Loizzo *et al.* 2016). Details about the sensor design can be found in Labate *et al.* (2009); Loizzo *et al.* (2016); Pignatti *et al.* (2015, 2013). PRISMA's on-board radiometric calibration system includes absolute calibration using the sun, relative calibration using two tungsten lamps, dark calibration using a shutter slit, and on-demand calibration using flat-field calibration and lunar observation (Pignatti *et al.* 2013). Stripes are removed using non-local means (Pignatti *et al.* 2015). Smile and keystone effects also exist, but errors are within 10% of a pixel (Labate *et al.* 2009). Clouds are detected using a discriminant analysis algorithm trained using Hyperion data (Pignatti *et al.* 2015). Atmospheric correction is done using a method similar to Moderate Resolution Atmospheric Transmission (Berk *et al.* 2008); a simplified radiative transfer equation, and a digital elevation model; for more detail on these pre-processing steps, please refer to Pignatti *et al.* (2015).

PRISMA collects data at 66 visible to near infrared (VNIR) bands from 400 to 1010 nm and 171 short-wave infrared (SWIR) bands from 920 to 2500 nm, at 10–12 nm spectral resolution (Loizzo *et al.* 2016; Pignatti *et al.* 2013). VNIR data are collected using a silicon-based detector, while SWIR data are collected using a mercury cadmium telluride diode array (Pignatti *et al.* 2013). In addition, PRISMA collects one panchromatic (PAN) band from 400 to 750 nm (Pignatti *et al.* 2013). The VNIR-SWIR imaging spectrometer and PAN camera are optically integrated to enable hyperspectral and panchromatic data fusion (Loizzo *et al.* 2016; Pignatti *et al.* 2015). Radiometric resolution is 12 bit, the swath width is 30 km, and the ground sampling distance is 30 m for VNIR-SWIR and 5 m for PAN (Loizzo *et al.* 2016). The SNR is greater than 200:1 in the 400 to 1750 nm range, and 100:1 at the 1950 to 2350 nm range (Loizzo *et al.* 2016). The PAN SNR is greater than 240:1 (Loizzo *et al.* 2016).

PRISMA data are available in several levels of processing (Loizzo *et al.* 2016). Level 0 consists of raw data with appended metadata (Loizzo *et al.* 2016). Level 1 consists of radiometrically corrected and calibrated top-of-atmosphere radiance, with masks for clouds, sunglint, and general classification (Loizzo *et al.* 2016). Level 2b consists of geolocated surface radiance (Loizzo *et al.* 2016). Level 2c consists of surface reflectance, with aerosol and water vapor products and cloud masks (Loizzo *et al.* 2016). Lastly, Level 2d consists of geocoded surface reflectance (Loizzo *et al.* 2016). ASI also plans to add subsequent product levels with geophysical, geochemical, biophysical, and biochemical characteristics (Loizzo *et al.* 2016).

Understanding the characteristics of these sensors is of great importance to advance science applications within and between sensors,

especially when integrating data from multiple hyperspectral sensors that will become available in the coming years. How do the spectral signatures of these multiple hyperspectral sensors compare with each other? What are their inter-relationships? How do they characterize different applications? What advances do they offer? These are relevant questions for which scientifically sound answers will allow full use of the new generation of hyperspectral data.

Hyperspectral Remote Sensing of Agriculture

Hyperspectral data provide several advantages over multispectral data in the study of agricultural crops because they provide information in hundreds of near-continuous bands along the electromagnetic spectrum; in contrast, multispectral data provide information in only a few broad spectral bands (Aneece and Thenkabail 2018; Kennedy *et al.* 2020; Lu *et al.* 2020; Thenkabail *et al.* 2021). HNB significantly improve classification accuracies of crop types, modeling of crop biochemical and biophysical characteristics, and assessment of other factors such as plant health and stress (Lu *et al.* 2020; Mariotto *et al.* 2013; Marshall *et al.* 2016; Thenkabail *et al.* 2018a, 2018b, 2018c, 2018d; Vali *et al.* 2020).

An extensive study of agricultural crops using hyperspectral remote sensing of old generation sensors has been documented in a four-volume book on the hyperspectral remote sensing of vegetation (Thenkabail *et al.* 2018a, 2018b, 2018c, 2018d). Many hyperspectral studies have been conducted using hand-held, truck-mounted, or airborne hyperspectral sensors. For example, several researchers have used airborne hyperspectral data to study agriculture (Feng *et al.* 2020; Nigam *et al.* 2019; Oki *et al.* 2006; Sahadevan 2021; Salas and Subburayalu 2019; Salas *et al.* 2020; Yang *et al.* 2021). However, these data may be more cost-prohibitive and/or more limited in spatial extent than satellite data. The first-of-its-kind NASA-built EO-1 Hyperion hyperspectral spaceborne sensor collected over 70 000 images across the world from 2001 to 2017 (Aneece and Thenkabail 2018). It was used for various agricultural applications like classification of crop residue, crop types and varieties, and crop conditions (Aneece and Thenkabail 2021; Bannari *et al.* 2015; Bhojaraja *et al.* 2015; Breunig *et al.* 2011; Lamparelli *et al.* 2012; Pan *et al.* 2013; Sonmez and Slater 2016) and for estimating tillage intensity and crop characteristics (Houborg *et al.* 2016; Mariotto *et al.* 2013; Marshall and Thenkabail 2015; Moharana and Dutta 2016; Sonmez and Slater 2016; Thenkabail *et al.* 2013), but has now been decommissioned.

We are now entering a new era of hyperspectral remote sensing with the launch of DESIS onboard ISS in 2018 and the polar-orbiting PRISMA in 2019. A few recent studies have used DESIS (Aneece and Thenkabail 2021) or PRISMA (Cogliati *et al.* 2021; Pepe *et al.* 2020) data to study agriculture. A few have also compared the two for geological (Tripathi and Garg 2021) and aquatic ecosystem applications (Bresciani *et al.* 2022). However, this is one of the first studies, alongside Hank *et al.* (2021), that compares the performance of DESIS and PRISMA in classifying agricultural crops. The differences in the bandwidths and spectral ranges of these sensors influence their use in various agricultural applications. In addition, these sensors are precursors to the recently launched German hyperspectral sensor Environmental Mapping and Analysis Program (EnMAP) and upcoming hyperspectral sensors like NASA's Surface Biology and Geology (SBG) mission. Thus, the study of these sensors will be invaluable once data from EnMAP, SBG, and others become available. One of the major advances of this study was building spectral libraries of major agricultural crops from these new generation sensors. Such libraries are important reference training and validation data for machine learning, deep learning, and artificial intelligence model development (Thenkabail *et al.* 2019). These models will in turn enable classification of crop types, estimation of biophysical and biochemical characteristics, and assessment of crop health and stress.

Overarching Goal and Objectives

The goal of this research was to study the characteristics of two new generation spaceborne hyperspectral sensors: DESIS and PRISMA. Two DESIS and one PRISMA images acquired during the 2020 growing season were used to classify seven major crops (almonds, corn, cotton, grapes, pistachios, rice, and tomatoes) in a study area located in the Central Valley of California, USA. Specific objectives were to:

1. Develop spectral libraries of seven major agricultural crops in California's Central Valley using DESIS (400–1000 nm) and PRISMA (400–2500 nm) new generation hyperspectral sensors;
2. Compare DESIS and PRISMA spectral characteristics of seven major crops in the 400 to 1000 nm spectral range;
3. Determine optimal hyperspectral narrowbands (OHNB) in DESIS and PRISMA data sets;
4. Establish crop type classification accuracies using OHNB from DESIS and PRISMA;
5. Develop and adapt hyperspectral narrowband vegetation indices based on literature review and OHNB.

Materials and Methods

Study Area

The study area is in the Central Valley of California, in north-central California (Figure 1). This area was selected due to the presence of several crop types in a small area that could be captured by DESIS and PRISMA image footprints, its significance in national food security, and image availability. We focused on almonds, corn, cotton, grapes, pistachios, rice, and tomatoes because these were most prevalent in the study area and/or are globally major crops. Planting and harvesting dates for these crops vary by year and farm. For example, corn is planted around May 15th and harvested around October 15th, but those dates can vary by plus or minus 1.5 months (Sacks *et al.* 2010). Similarly, cotton is planted around April 20th and harvested around October 25th and rice is planted around May 15th and harvested around October 10th, but these dates vary by plus or minus one month (Sacks *et al.* 2010). Tomatoes are planted around April 1st and harvested before the first frost around December 1st (California Grown, 2022). Almonds, pistachios, and grapevines grow throughout the year. Almonds are harvested August through November, pistachios September through November, and grapes July through November (CUESA, 2022). Below, we describe the hyperspectral data acquired for this study area (Figure 1), followed by reference and validation data.

Data

The goal of this research was to compare two new generation sensors (DESIS and PRISMA), both of which need to be tasked for acquiring

data rather than providing wall-to-wall coverage as do satellites like Landsat. Getting images over the same area on the same or similar dates is extremely difficult. A study of this nature, however, requires acquisitions on the same or similar dates to build a valid comparison. We were able to achieve this for our study area by acquiring data from DESIS onboard the ISS and PRISMA, a polar-orbiting satellite, by tasking them. Both satellites acquired some images for the study area; we reviewed them and selected those of good quality, similar dates of acquisition within the growing season, and with overlapping footprints. Therefore, three hyperspectral images over the study area were selected with which we were able to compare DESIS and PRISMA images for similar dates, and DESIS June with DESIS August images to assess crops in different growth stages. The two DESIS images were acquired in clear conditions on June 18, 2020, and August 8, 2020, downloaded as Level 2a, surface reflectance products from DLR and Teledyne Brown (German Aerospace Center (formerly DLR) and Teledyne Brown 2022). The PRISMA image with less than 11.5% cloud cover was acquired on June 17, 2020 and downloaded as a Level 2D surface reflectance product from the PRISMA data portal made available by the ASI (Italian Space Agency (ASI) 2022).

The United States Department of Agriculture's National Agricultural Statistics Service Cropland Data Layer (USDA NASS CDL) (USDA National Agricultural Statistics Service Cropland Data Layer 2022) was used as reference data because it consists of yearly wall-to-wall crop type data for the USA. The USDA NASS CDL has relatively high classification accuracies for the selected study crops in the study site (Table 2; USDA NASS 2022) and has been used frequently in research for reference (Boryan and Yang 2021; Hao *et al.* 2016; Lark *et al.* 2021; Zhang *et al.* 2021a; Zhong *et al.* 2014). As seen in Table 2, all study crops except for corn and grapes have high producer's (87.9%–97.7%), user's (82.7%–99.1%) accuracies, and Kappa values (0.876–0.975) (USDA NASS 2022). While lower than the others, corn and grapes also have relatively high producer's accuracies (74.8% and 77.7%, respectively), user's accuracies (80.5% and 71.2%, respectively) accuracies, and Kappa values (0.744 and 0.774, respectively) (USDA NASS 2022). These two crop types also covered less area than the other study crop types. Thus, we used the high-quality USDA NASS CDL data for reference.

Because the three images had a slight spatial misalignment, we georeferenced them to the USDA NASS CDL in ArcGIS (Version 10.8.1; ESRI 2022) to ensure sampling at the same location across images. The image footprints had enough overlap to select samples across all three images. Sampling was done by generating random points within the overlapping area with a minimum distance of 100 m to avoid autocorrelation and extracting data from all three images. This sampling was also done in ArcGIS (Version 10.8.1; ESRI 2022).

In addition to extracting crop type data (illustrated in Figure 2), confidence information was also extracted from the USDA NASS CDL (USDA National Agricultural Statistics Service Cropland Data Layer 2022). The random samples were then filtered based on confidence, crop type (only retaining study crops), and spectral quality (Table 3). We retained only samples with confidence levels of at least 70%. A lower threshold allowed the introduction of noise and a higher threshold impeded adequate sample size. Fields with double-cropping were excluded to ensure spectral

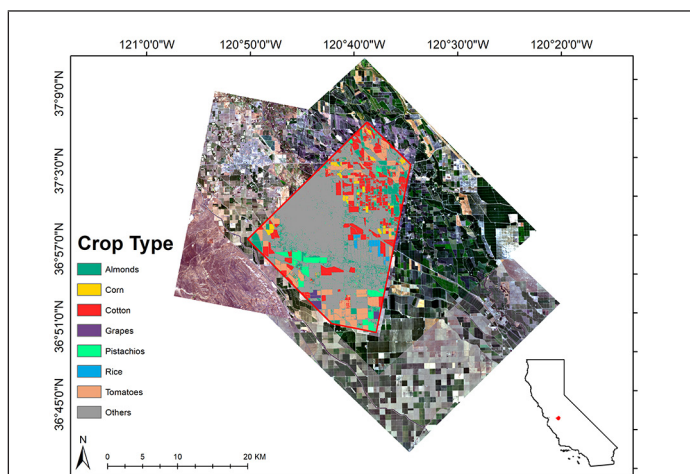


Figure 1. Study area. Location of the study area showing PRerecursore IperSpettrale della Missione Applicativa (PRISMA) and Deutsches Zentrum für Luft- und Raumfahrt (DLR) Earth Sensing Imaging Spectrometer (DESIS) image footprints. The red outline indicates overlapping area across all three images. A PRISMA image from June 17, 2020, and two DESIS images from June 18, 2020, and August 8, 2020, were acquired in California's Central Valley. Within the outline is the United States Department of Agriculture Cropland Data Layer showing study crop type distributions for the 2020 growing season. [Source: USDA National Agricultural Statistics Service Cropland Data Layer (2022)].

Table 2. Classification accuracies and Kappa statistics from the United States Department of Agriculture National Agricultural Statistics Service Cropland Data Layer (USDA National Agricultural Statistics Service Cropland Data Layer, 2022) for 2020 in California for the study crops. [Source: (USDA NASS 2022)]

Crop Type	Producer's Accuracy (%)	User's Accuracy (%)	Kappa
Almonds	89.2	87.9	0.884
Corn	74.8	80.5	0.744
Cotton	87.9	86.6	0.876
Grapes	77.7	71.2	0.774
Pistachios	88.6	89.7	0.883
Rice	97.7	99.1	0.975
Tomatoes	88.2	82.7	0.879
Average	86.3	85.4	0.859

signatures were as pure as possible. Data used in this study are available through the ScienceBase Catalog (Aneece and Thenkabail 2022).

Sensor Comparisons

Spectral libraries were used to generate correlation plots in R (Version 4.0.4; R Core Team 2018) using the ggplot2 package (Version 3.3.5; Wickham 2016) comparing DESIS and PRISMA June spectral reflectances at various wavelength ranges: 400 to 1000 nm, 400 to 699 nm, 700 to 759 nm, 760 to 899 nm, and 900 to 1000 nm. Correlation analysis was done within and across crop types. Since only June PRISMA data were available, only June DESIS data were included in this analysis. To establish a fair comparison, broader DESIS bands were simulated by averaging across five bands to approximate PRISMA bandwidths. Linear models were determined in R (Version 4.0.4; R Core Team 2018) using the ggmisc package (Aphalo 2020). Band averaging was only done for these correlation analyses, not for the optimal band selection or classification analyses described below.

Optimal Bands

Many methods for band selection exist, including principal component analyses, lambda-by-lambda plots, and stepwise-regression (Aneece and Thenkabail 2021; Mariotto *et al.* 2013; Marshall *et al.* 2016). In this study, we selected optimal HNB for DESIS and PRISMA data using peak and trough detection, which has successfully been used for finding features in other remote sensing applications (Ali and Clausi 2001; Kutser *et al.* 2016; Zarco-Tejada *et al.* 2003). First, peaks and troughs were determined by comparing the reflectance of a band with the reflectances of bands immediately before and immediately after it. This comparison was done separately for each hyperspectral image and each crop type. We counted the number of times each peak or trough wavelength was detected by month and crop type. The most frequently detected wavelengths across images and crop types, which represented consistent patterns at specific locations of the spectrum, were selected for future analysis. Frequencies varied by month and crop type; thus, a single threshold value could not be used. To determine the most important bands for DESIS analysis, we pooled June and August data. Since PRISMA data were only available for June, these were used to determine the most important bands.

Classification Algorithms

The support vector machine supervised classification algorithm was selected to classify crop types and compare classification accuracies across sensors. This algorithm has been used successfully for hyperspectral (including DESIS) analysis (Aneece and Thenkabail 2021; Gopinath *et al.* 2020; Lin and Yan 2016; Praveen *et al.* 2016; Puletti *et al.* 2016; Rodriguez-Galiano *et al.* 2015), and has outperformed random forest for hyperspectral crop classification (Aneece and Thenkabail 2018, 2021). The linear kernel produced higher accuracies than the more commonly used radial basis function kernel and was thus selected for this analysis.

To compare the abilities of DESIS and PRISMA data to classify agricultural crop types, we conducted classification analyses using the following:

1. 26 DESIS bands at 2.55 nm from 400 to 1000 nm
2. 25 PRISMA bands at ≤ 12 nm from 400 to 1000 nm
3. 45 PRISMA bands at ≤ 12 nm from 400 to 2500 nm

Classification comparisons using the first and second data sets would help detect any benefits the narrower DESIS bands may provide over the relatively broader PRISMA bands. A comparison between results using the second and third data sets would help detect the advantages of including SWIR data in classification of these crop types.

Vegetation Indices

PRISMA OHNB were used to adapt vegetation indices found in literature based on narrowbands available in PRISMA data, the optimal band analysis in this study, and extensive literature review (Carter 1994; Clevers 2014; Daughtry 2001; Giovos *et al.* 2021; Gitelson *et al.* 2006, 2001, 2002; Hatfield *et al.* 2019; Hunt *et al.* 2013; Kandalakis and Karantzalos 2016; Kior *et al.* 2021; Lichtenthaler *et al.* 1996; Poley and McDermid 2020; Roberts *et al.* 2018; Segarra *et al.* 2020; Serrano *et al.* 2002; Vogelmann *et al.* 1993; Wang and Qu 2007; Zarco-Tejada *et al.* 2005; Zhang *et al.* 2021b). OHNB were also used to build hyperspectral two-band vegetation indices (HTBVI), which may be used to estimate crop characteristics such as plant pigment content, biomass, stress,

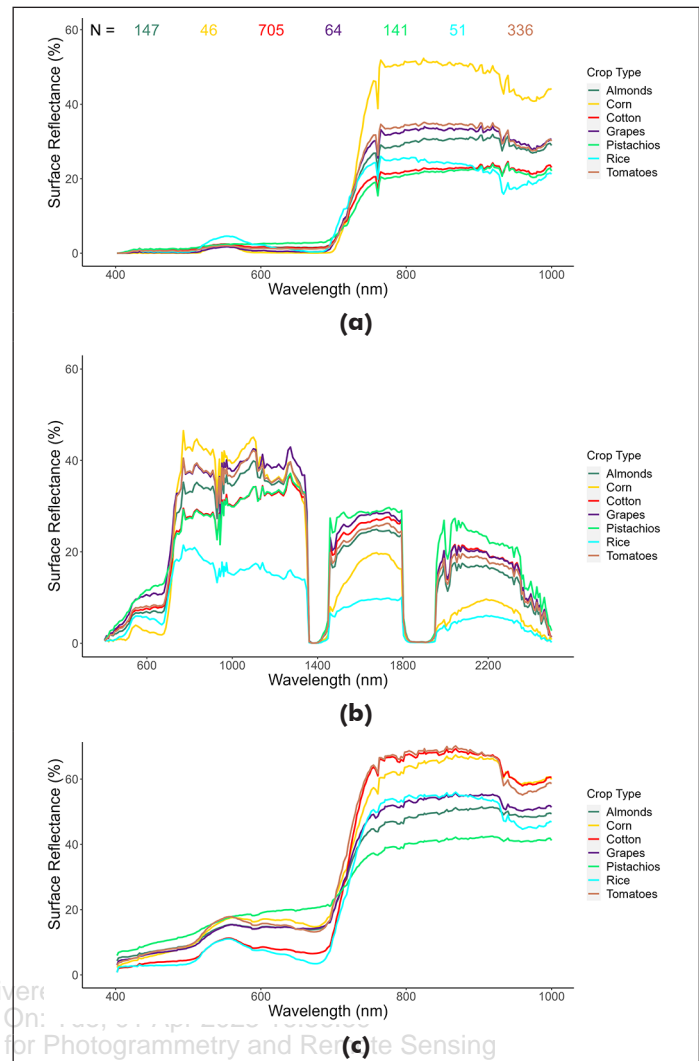


Figure 2. Spectral libraries of study crops. (a) Deutsches Zentrum für Luft- und Raumfahrt (DLR) Earth Sensing Imaging Spectrometer (DEIS) June, (b) PRecursore IperSpettrale della Missione Applicativa (PRISMA) June, and (c) DESIS August spectra, averaged by crop type. The number of spectra (N) used to calculate the average is the same for all three plots.

Table 3. Number of samples used in this study. Reference crop type data were extracted from the United States Department of Agriculture National Agricultural Statistics Service Cropland Data Layer (USDA National Agricultural Statistics Service Cropland Data Layer, 2022).

Crop Type	Number of Samples			
	Training	Testing	Validation	Total
Almonds	74	36	37	147
Corn	23	12	11	46
Cotton*	50	25	25	705
Grapes	32	16	16	64
Pistachios	70	36	35	141
Rice	26	12	13	51
Tomatoes*	50	25	25	336
Total	325	162	162	1490

*For classification, 100 spectra were randomly selected to balance sample sizes across crop types.

and moisture. The HTBVI can be calculated using Equation 1, where $R_{\lambda 1}$ and $R_{\lambda 2}$ are percent surface reflectances at wavelengths $\lambda 1$ and $\lambda 2$, respectively.

$$HTBVI = \frac{R_{\lambda 1} - R_{\lambda 2}}{R_{\lambda 1} + R_{\lambda 2}} \quad (1)$$

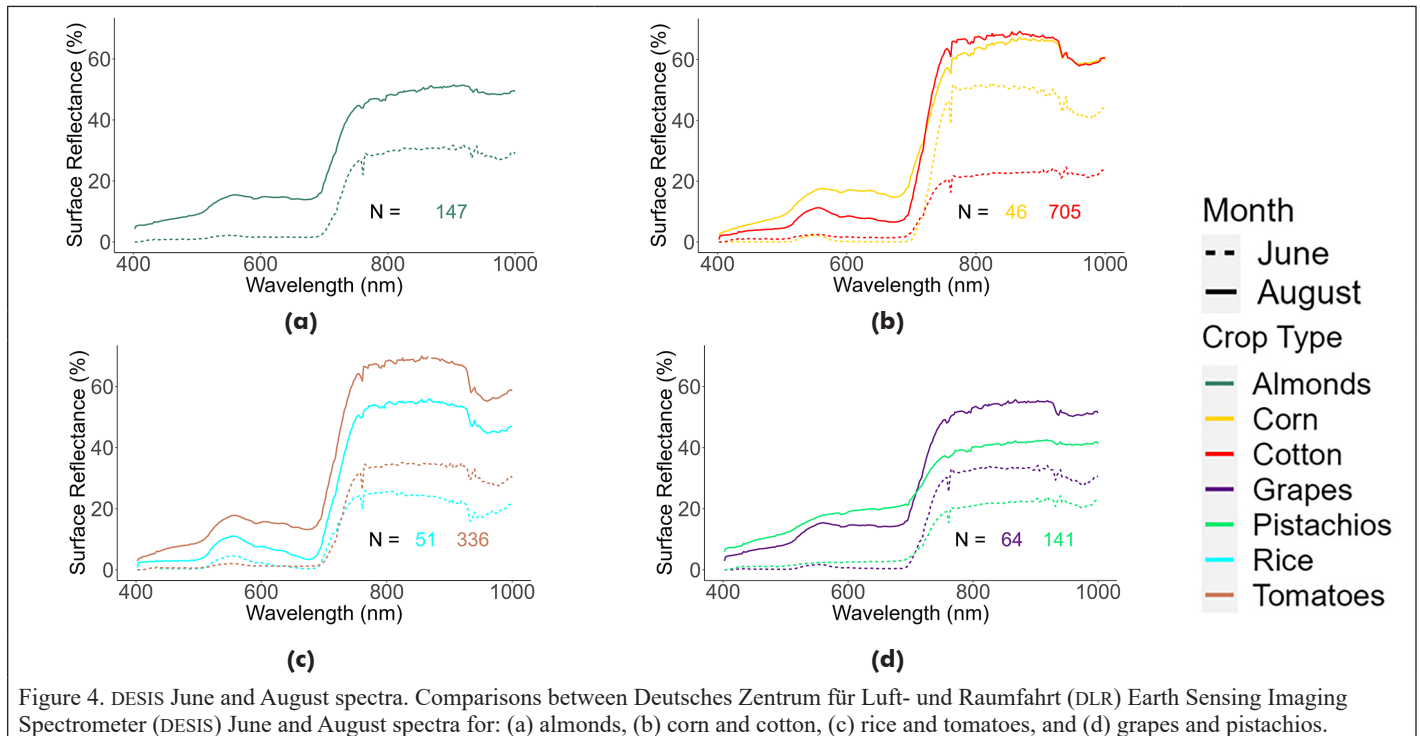
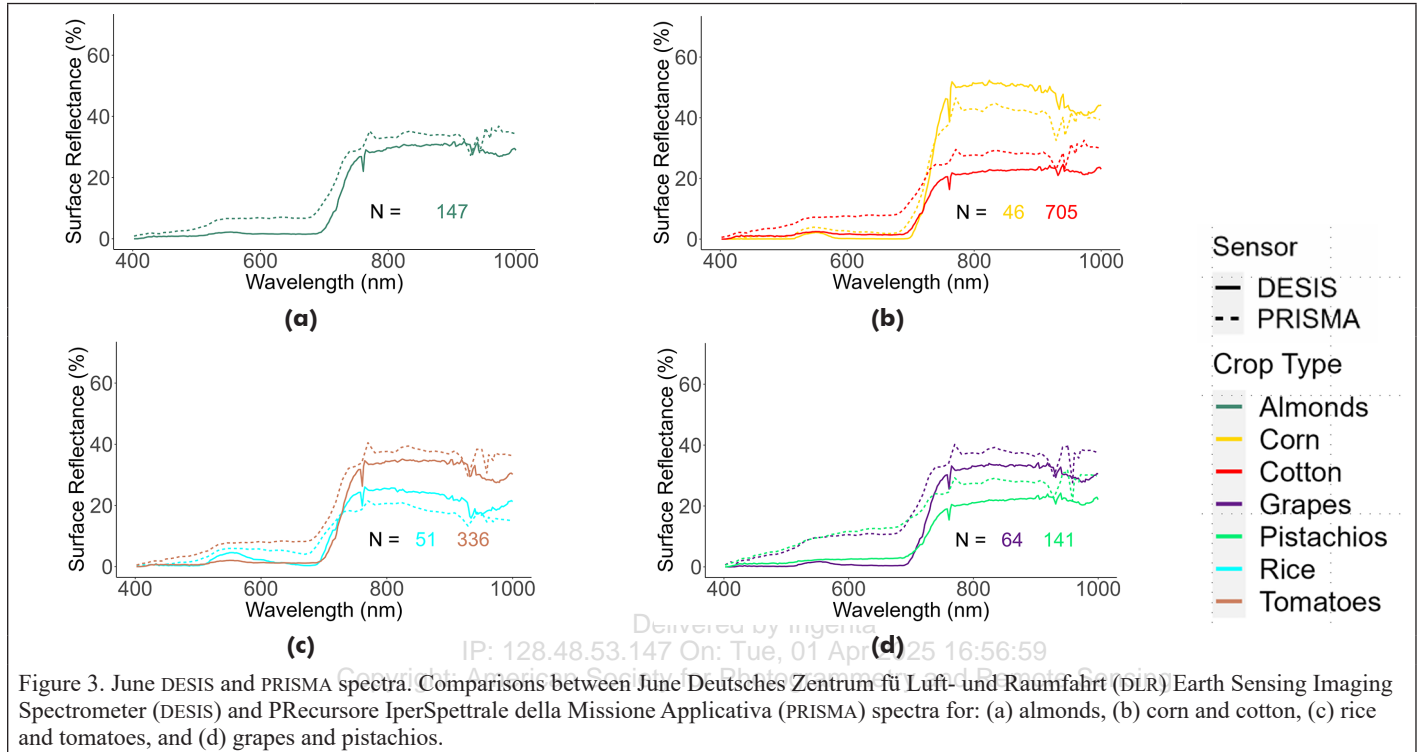
Results

Sensor Comparisons

As shown in Figure 3, PRISMA and DESIS data in the early growing season (June) had similarly shaped spectral profiles of crops in early vegetative growth. However, PRISMA average reflectances were higher than DESIS for all crops in the visible range, and for most crops in the near-infrared (NIR) range. In contrast, the NIR reflectances for corn and

rice were higher in DESIS data than PRISMA. Additionally, the shapes of the spectral profiles in the water absorption trough from 900 to 1000 nm differed between sensors. Average PRISMA spectral profiles were also smoother than DESIS profiles due to wider bands.

When comparing the two DESIS images, one in June and one in August, the August reflectances were higher than June reflectances as would be expected later in the growing season (Figure 4). Also as expected, the green peaks, red troughs, and water absorption features (from plant moisture) were more prominent later in the growing season. Subtle spectral features in the red (600 to 670 nm) and NIR (800 to 900 nm) ranges were also more prominent in August spectra.



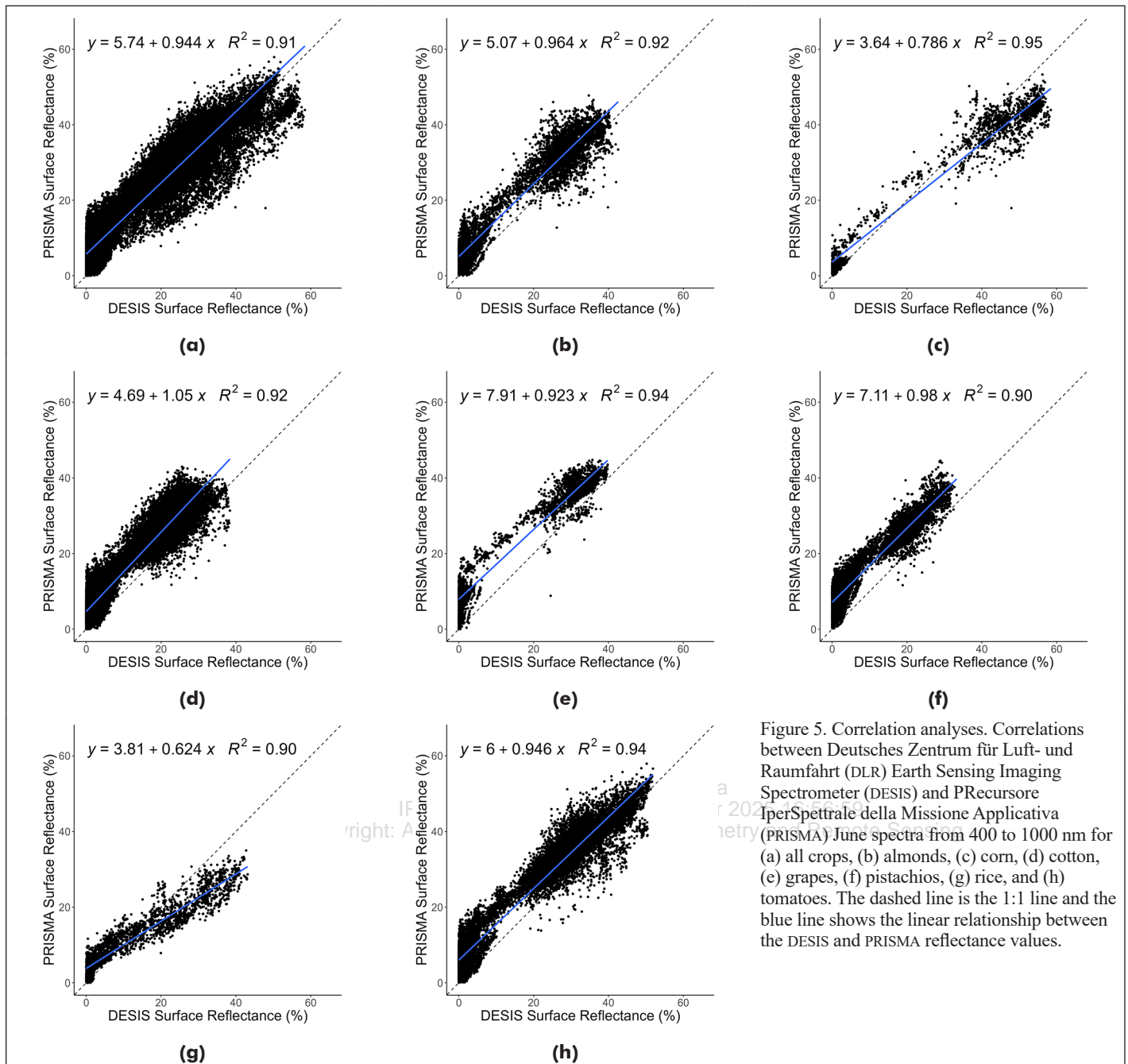


Figure 5. Correlation analyses. Correlations between Deutsches Zentrum für Luft- und Raumfahrt (DLR) Earth Sensing Imaging Spectrometer (DESIS) and PRecursoRe IperSpettrale della Missione Applicativa (PRISMA) June spectra from 400 to 1000 nm for (a) all crops, (b) almonds, (c) corn, (d) cotton, (e) grapes, (f) pistachios, (g) rice, and (h) tomatoes. The dashed line is the 1:1 line and the blue line shows the linear relationship between the DESIS and PRISMA reflectance values.

In addition to the visual comparisons described below, linear correlation analyses were run between PRISMA and DESIS June spectra (Figure 5 and Table 4). When considering the entire 400 to 1000 nm spectral range, R^2 values ranged from 0.90 to 0.95 across crop types. Correlations were also strong in the 700 to 759 nm range, with R^2 values of 0.77 to 0.94. In contrast, correlations were relatively weak in the 400 to 699 nm range, with R^2 values of 0.11 to 0.44 across crop types, as well as in the 900 to 1000 nm range, with R^2 values of 0.12 to 0.49 for all crops except rice (R^2 0.81). Finally, R^2 values varied from 0.40 to 0.83 in the 760 to 899 nm range.

Optimal Bands

Out of the 235 DESIS bands in the 400 to 1000 nm range, 26 bands (11%) were selected for further analysis, as illustrated in Figure 6 and Table 5. These band center wavelengths have been found useful for various agricultural applications (Anece and Thenkabail 2021; Mariotto *et al.* 2013; Thenkabail 2015; Thenkabail *et al.* 2021, 2014) including crop type and growth stage classification, disease and stress detection, estimation of biochemical properties such as nitrogen,

Table 4. Coefficients of determination (R^2) for Deutsches Zentrum für Luft- und Raumfahrt (DLR) Earth Sensing Imaging Spectrometer (DESIS) and PRecursoRe IperSpettrale della Missione Applicativa (PRISMA) spectral comparisons.

Crop(s)	Spectral Range				
	400–1000 nm	400–699 nm	700–759 nm	760–899 nm	900–1000 nm
All	0.91	0.25	0.78	0.75	0.53
Almonds	0.92	0.28	0.81	0.47	0.17
Corn	0.95	0.11	0.94	0.40	0.16
Cotton	0.92	0.24	0.77	0.61	0.36
Grapes	0.94	0.13	0.93	0.75	0.12
Pistachios	0.90	0.43	0.78	0.79	0.45
Rice	0.90	0.44	0.82	0.83	0.81
Tomatoes	0.94	0.27	0.89	0.78	0.49

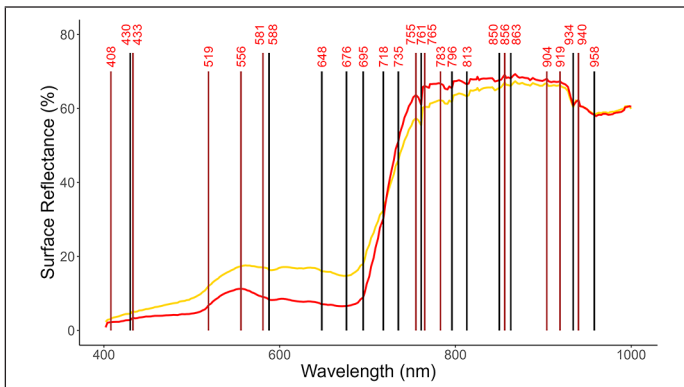


Figure 6. DESIS OHNB. Deutsches Zentrum für Luft- und Raumfahrt (DLR) Earth Sensing Imaging Spectrometer (DESIS) optimal hyperspectral narrowbands (OHNB), represented by vertical lines along corn (yellow) and cotton (red) spectra. Brown vertical lines represent peaks while black vertical lines represent troughs.

pigment, protein, and moisture content, and biophysical properties such as biomass/yield (sometimes estimated using Leaf Area Index (LAI)), and vegetation vigor.

Out of the 238 PRISMA bands from 400 to 2500 nm, 45 bands (19%) were selected as optimal for agricultural studies, as illustrated in Figures 7 and 8 and listed in Table 6 (see page 723). As with the selected DESIS bands, these bands have been used for differentiating crop and vegetation types, their growth stages, weeds, and diseased and stressed plants, for estimating crop biomass/yield (and LAI), nitrogen, protein, pigment, water, starch, sugar, cellulose, and lignin content, and for assessing Light Use Efficiency (LUE) (Aneece and Thenkabail 2018, 2021; Delalieux *et al.* 2007; Mariotto *et al.* 2013; Thenkabail *et al.* 2021). Of the selected 45 bands, 25 are within the 400 to 1000 nm range, almost the same number of bands selected from DESIS data along the same spectral range.

Classification Accuracies

The selected OHNB of DESIS and PRISMA in the 400 to 1000 nm range achieved the best results in classifying the seven agricultural crops, with the higher PRISMA overall accuracy of 90% compared to the DESIS

Table 5. Characteristics and relevance of Deutsches Zentrum für Luft- und Raumfahrt (DLR) Earth Sensing Imaging Spectrometer (DESIS) optimal hyperspectral narrowbands.

λ (nm)	Frequency	Feature	Relevance	References
408	99	Peak	Nitrogen, senescence	Thenkabail (2015); Thenkabail <i>et al.</i> (2014)
430	263	Trough	Crop classification, biomass/yield, chlorophyll	Mariotto <i>et al.</i> (2013); Mobasheri and Rahimzadegan (2012)
433	245	Peak	Crop classification, chlorophyll	Mariotto <i>et al.</i> (2013); Mobasheri and Rahimzadegan (2012)
519	8	Peak	Pigment, biomass change	Thenkabail <i>et al.</i> (2021)
556	4	Peak	Nitrogen, growth stage, weeds, pigments	Aneece and Thenkabail (2021); Hennessy <i>et al.</i> (2020); Ma <i>et al.</i> (2019); Mudereri <i>et al.</i> (2020); Ren <i>et al.</i> (2020); Salem <i>et al.</i> (2017); Thenkabail <i>et al.</i> (2021)
581	42	Peak	Vegetation vigor, pigments, nitrogen	Thenkabail <i>et al.</i> (2021)
588	25	Trough	Biomass/yield	Aneece and Thenkabail (2021); Mariotto <i>et al.</i> (2013); Ren <i>et al.</i> (2020)
648	124	Trough	Biomass/yield, chlorophyll	Aneece and Thenkabail (2021); Clevers (2014); Mobasheri and Rahimzadegan (2012); Ren <i>et al.</i> (2020); Thenkabail <i>et al.</i> (2013)
676	11	Trough	Biomass/yield, disease, pigments, weeds, LAI	Aneece and Thenkabail (2018, 2021); Chen <i>et al.</i> (2020); Deng <i>et al.</i> (2020); Mudereri <i>et al.</i> (2020); Roberts <i>et al.</i> (2018); Salem <i>et al.</i> (2017)
695	180	Trough	Stress, chlorophyll, biomass, LAI	Thenkabail <i>et al.</i> (2021, 2004)
718	148	Trough	Stress, pigments, growth stage	Aneece and Thenkabail (2018, 2021); Ma <i>et al.</i> (2019); Thenkabail <i>et al.</i> (2014, 2013)
735	292	Trough	Nitrogen, LULC classification, growth stage, LAI	Aneece and Thenkabail (2021); Chen <i>et al.</i> (2020); Ma <i>et al.</i> (2019); Ren <i>et al.</i> (2020); Thenkabail <i>et al.</i> (2021)
755	10	Peak	Biomass/yield, pigments	Aneece and Thenkabail (2018, 2021); Mariotto <i>et al.</i> (2013); Ren <i>et al.</i> (2020); Salem <i>et al.</i> (2017); Thenkabail <i>et al.</i> (2013)
761	865	Trough	Biomass/yield, pigments	Aneece and Thenkabail (2018, 2021); Ren <i>et al.</i> (2020); Salem <i>et al.</i> (2017); Thenkabail <i>et al.</i> (2013)
765	379	Peak	Biomass/yield, pigments	Aneece and Thenkabail (2018, 2021); Ren <i>et al.</i> (2020); Salem <i>et al.</i> (2017); Thenkabail <i>et al.</i> (2013)
783	36	Peak	Biomass/yield, crop classification	Aneece and Thenkabail (2021); Mariotto <i>et al.</i> (2013); Ren <i>et al.</i> (2020)
796	87	Trough	Biomass/yield, crop classification	Aneece and Thenkabail (2021); Mariotto <i>et al.</i> (2013); Ren <i>et al.</i> (2020)
813	17	Trough*	Crop classification	Mariotto <i>et al.</i> (2013)
850	359	Trough*	Biophysical characteristics, pigments	Thenkabail <i>et al.</i> (2021, 2004)
856	273	Peak**	Biomass/yield, pigments, disease, LAI	Aneece and Thenkabail (2018, 2021); Chen <i>et al.</i> (2020); Deng <i>et al.</i> (2020); Thenkabail <i>et al.</i> (2014, 2013)
863	361	Trough	Crop classification	Aneece and Thenkabail (2021); Mariotto <i>et al.</i> (2013); Zhang <i>et al.</i> (2018)
904	156	Peak	Biomass/yield, pigments, LAI, proteins	Aneece and Thenkabail (2021); Mariotto <i>et al.</i> (2013); Mobasheri and Rahimzadegan (2012); Thenkabail <i>et al.</i> (2004, 2013); Zhang <i>et al.</i> (2018)
919	377	Peak	Moisture, biomass, proteins	Thenkabail <i>et al.</i> (2021)
934	885	Trough	Biomass/yield, LAI, oils	Aneece and Thenkabail (2021); Chen <i>et al.</i> (2020); Mariotto <i>et al.</i> (2013); Mobasheri and Rahimzadegan (2012)
940	684	Peak	Biomass/ yield, LAI, moisture	Aneece and Thenkabail (2021); Chen <i>et al.</i> (2020); Clevers (2014); Mariotto <i>et al.</i> (2013); Thenkabail <i>et al.</i> (2004)
958	370	Trough	Moisture, biomass/yield, protein, growth stage	Aneece and Thenkabail (2021); Chen <i>et al.</i> (2020); Ma <i>et al.</i> (2019); Thenkabail <i>et al.</i> (2014, 2013)

LAI = Leaf Area Index; LULC = Land Use/Land Cover.

*Local peak within larger trough; **Local trough within larger peak.

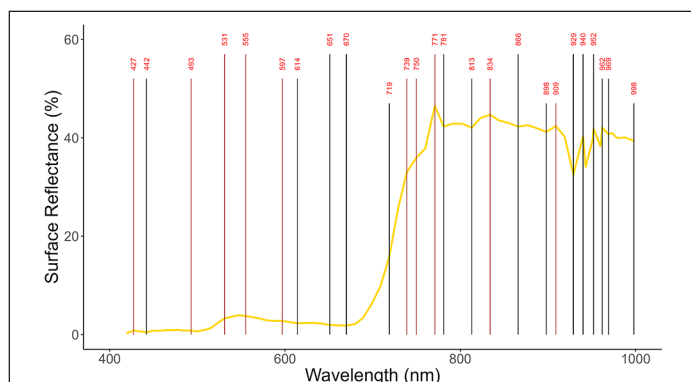


Figure 7. PRISMA OHNB 400–1000 nm. PRecurso IperSpettrale della Missione Applicativa (PRISMA) optimal hyperspectral narrowbands (OHNB) from 400 to 1000 nm, represented by vertical lines along corn spectra. Brown vertical lines represent peaks while black vertical lines represent troughs.

overall accuracy of 83% (Table 7). Producer's accuracies for PRISMA ranged from 72–100%, while user's accuracies ranged from 80–100%. Those for DESIS ranged from 63–100% and 67–100%, respectively. Especially of note are the much lower user's accuracy for almonds and producer's accuracy for grapes using DESIS data, caused by grape spectra being misclassified as almonds. This may be due to the spectral similarities of the two for DESIS data, and due to the small area of grapes and large area of almonds in the study area.

However, including PRISMA bands beyond 1000 nm did not result in increased classification accuracies, with an overall accuracy of 89% compared to 90% using only bands from 400 to 1000 nm (Table 7). Using all bands resulted in producer's accuracies of 72–100% and user's accuracies of 73–100%. However, the bands beyond 1000 nm are useful for estimating specific crop biophysical and biochemical properties (Giovos *et al.* 2021; Hatfield *et al.* 2019; Kior *et al.* 2021; Roberts *et al.* 2018).

Vegetation Indices

Since classification accuracies were higher using PRISMA OHNB than when using DESIS OHNB, we focused on using PRISMA bands to build vegetation indices. Out of numerous existing vegetation indices, we selected some of the commonly used indices to estimate plant biomass/density/yield; nitrogen, pigment, moisture, and structural content; and stress (Table 8, see page 724). These were adapted to PRISMA data considering bands used in literature review and spectral features seen in PRISMA data. In addition to adapting existing vegetation indices, we

Table 7. Classification accuracies for Deutsches Zentrum für Luft- und Raumfahrt (DLR) Earth Sensing Imaging Spectrometer (DESI) optimal hyperspectral narrowbands (OHNB), PRecurso IperSpettrale della Missione Applicativa (PRISMA) OHNB from 400 to 1000 nm, and PRISMA OHNB from 400 to 2500 nm using support vector machine (Anece and Thenkabail 2021) classification.

Crop Type	Producer's (User's) Accuracy (%)		
	DESI	PRISMA_400 to 1000	PRISMA_400 to 2500
Almonds	92 (67)	92 (87)	84 (97)
Corn	100 (100)	100 (100)	100 (100)
Cotton	80 (91)	72 (90)	72 (95)
Grapes	63 (77)	75 (92)	81 (87)
Pistachios	86 (94)	94 (97)	97 (89)
Rice	100 (100)	100 (87)	100 (93)
Tomatoes	68 (85)	96 (80)	96 (73)
Overall Accuracy (%)	83	90	89

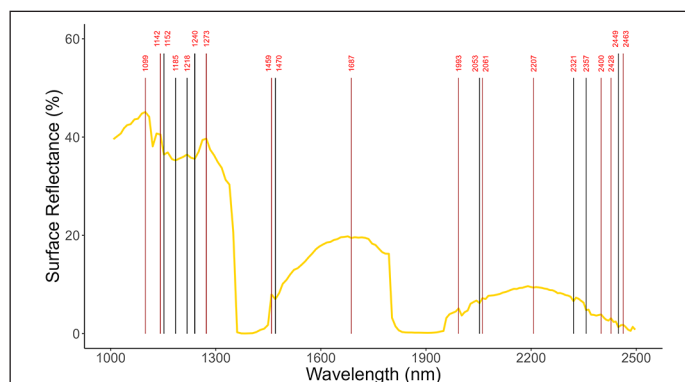


Figure 8. PRISMA OHNB 1000–2500 nm. PRecurso IperSpettrale della Missione Applicativa (PRISMA) optimal hyperspectral narrowbands (OHNB) from 1000 to 2500 nm, represented by vertical lines along corn spectra. Brown vertical lines represent peaks while black vertical lines represent troughs.

have suggested HTBVI that may be useful for estimating such biophysical and biochemical characteristics as plant pigment, stress, biomass, moisture, and cellulose/lignin (Table 9).

Discussion

In this paper, we compared data from the new generation hyperspectral sensors PRISMA and DESIS using two DESIS images and one PRISMA image in the growing season of 2020 in the Central Valley of California, USA. We developed spectral libraries for each sensor for seven major

Table 9. Potential PRecurso IperSpettrale della Missione Applicativa (PRISMA) hyperspectral optimal two-band pairs for the hyperspectral two-band vegetation indices (HTBVI) determined in this study.

λ_1 (nm)	λ_2 (nm)	HTBVI* (Unitless)	Potential Characteristics
555	670	HTBVI-1	Pigment content (Anthocyanin, Chlorophyll, Carotenoids)
555	493	HTBVI-2	
555	614	HTBVI-3	
427	670	HTBVI-4	
719	670	HTBVI-5	Plant stress in visible region
771	719	HTBVI-6	
771	670	HTBVI-7	Wet and dry biomass, Leaf Area Index, plant height, plant density
771	781	HTBVI-8	
834	813	HTBVI-9	
771	969	HTBVI-10	Plant moisture, water content
771	929	HTBVI-11	
834	969	HTBVI-12	
834	929	HTBVI-13	
834	998	HTBVI-14	
1099	1185	HTBVI-15	
1099	998	HTBVI-16	
1099	1240	HTBVI-17	Plant cellulose and/or lignin content
1273	1185	HTBVI-18	
1142	1152	HTBVI-19	
1273	1240	HTBVI-20	Plant stress in shortwave infrared region
1459	1470	HTBVI-21	
1687	1470	HTBVI-22	
2061	2053	HTBVI-23	
2207	2053	HTBVI-24	
2207	2357	HTBVI-25	
2400	2449	HTBVI-26	

*HTBVI = $(R_{\lambda_1} - R_{\lambda_2}) / (R_{\lambda_1} + R_{\lambda_2})$.

Table 6. Characteristics and relevance of *PR*ecursore *I*perSpettrale della *M*issione *A*pplicativa (PRISMA) optimal hyperspectral narrowbands.

λ (nm)	Frequency	Feature	Relevance	Reference
427	287	Peak	Crop classification, biomass/yield, chlorophyll	Mariotto <i>et al.</i> (2013); Mobasheri and Rahimzadegan (2012)
442	351	Trough	Nitrogen, senescing, chlorophyll	Aneece and Thenkabail (2018); Clevers (2014); Thenkabail <i>et al.</i> (2013)
493	4	Peak*	Carotenoids, LUE, stress	Aneece and Thenkabail (2018); Hennessy <i>et al.</i> (2020); Thenkabail <i>et al.</i> (2014, 2013)
531	18	Peak	LUE, stress, disease, growth stage	Aneece and Thenkabail (2021); Deng <i>et al.</i> (2020); Hennessy <i>et al.</i> (2020); Ma <i>et al.</i> (2019); Ren <i>et al.</i> (2020); Roberts <i>et al.</i> (2018); Thenkabail <i>et al.</i> (2014, 2013)
555	11	Peak*	Nitrogen, growth stage, weeds, pigments	Aneece and Thenkabail (2021); Hennessy <i>et al.</i> (2020); Ma <i>et al.</i> (2019); Mudereri <i>et al.</i> (2020); Ren <i>et al.</i> (2020); Salem <i>et al.</i> (2017); Thenkabail <i>et al.</i> (2021)
597	17	Peak	LULC classification	Aneece and Thenkabail (2021); Mariotto <i>et al.</i> (2013); Ren <i>et al.</i> (2020)
614	50	Trough	LULC classification, biomass, LAI	Aneece and Thenkabail (2021); Chen <i>et al.</i> (2020); Ren <i>et al.</i> (2020); Thenkabail <i>et al.</i> (2004); Zhang <i>et al.</i> (2018)
651	61	Trough	Biomass/yield, chlorophyll	Aneece and Thenkabail (2021); Clevers (2014); Ren <i>et al.</i> (2020); Thenkabail <i>et al.</i> (2013)
670	45	Trough	Biomass/yield, disease, pigments, weeds, LAI	Aneece and Thenkabail (2018, 2021); Chen <i>et al.</i> (2020); Deng <i>et al.</i> (2020); Mudereri <i>et al.</i> (2020); Roberts <i>et al.</i> (2018); Salem <i>et al.</i> (2017)
719**	0	Trough	Stress, pigments, growth stage	Aneece and Thenkabail (2018, 2021); Ma <i>et al.</i> (2019); Thenkabail <i>et al.</i> (2014, 2013)
739	119	Peak	Nitrogen, LULC classification, growth stage, LAI	Aneece and Thenkabail (2021); Chen <i>et al.</i> (2020); Ma <i>et al.</i> (2019); Ren <i>et al.</i> (2020); Thenkabail <i>et al.</i> (2021)
750	300	Peak*	Biomass/yield, pigments	Aneece and Thenkabail (2018, 2021); Mariotto <i>et al.</i> (2013); Ren <i>et al.</i> (2020); Salem <i>et al.</i> (2017); Thenkabail <i>et al.</i> (2013)
771	1484	Peak	Biomass/yield, LAI	Aneece and Thenkabail (2018)
781	792	Trough	Biomass/yield, crop classification	Aneece and Thenkabail (2021); Mariotto <i>et al.</i> (2013); Ren <i>et al.</i> (2020)
813	614	Trough	Crop classification	Mariotto <i>et al.</i> (2013)
834	625	Peak*	Biomass/yield	Aneece and Thenkabail (2021); Mariotto <i>et al.</i> (2013)
866	827	Trough	Crop classification	Aneece and Thenkabail (2021); Mariotto <i>et al.</i> (2013); Zhang <i>et al.</i> (2018)
898	1047	Trough	Biomass/yield, pigments, LAI, proteins	Aneece and Thenkabail (2021); Mariotto <i>et al.</i> (2013); Thenkabail <i>et al.</i> (2004, 2013); Zhang <i>et al.</i> (2018)
909	1136	Peak	Biomass/yield, pigments, protein	Aneece and Thenkabail (2021); Mobasheri and Rahimzadegan (2012); Thenkabail <i>et al.</i> (2013); Zhang <i>et al.</i> (2018)
929	1488	Trough	Biomass/yield, LAI, oils	Aneece and Thenkabail (2018); Mobasheri and Rahimzadegan (2012)
940	1467	Trough***	Biomass/yield, LAI, water content	Aneece and Thenkabail (2021); Chen <i>et al.</i> (2020); Clevers (2014); Mariotto <i>et al.</i> (2013); Thenkabail <i>et al.</i> (2004)
952	1400	Trough***	Biomass/yield	Mariotto <i>et al.</i> (2013)
962	1084	Trough***	Moisture, biomass/yield, protein, growth stage, LAI	Aneece and Thenkabail (2021); Chen <i>et al.</i> (2020); Ma <i>et al.</i> (2019); Roberts <i>et al.</i> (2018); Thenkabail <i>et al.</i> (2014, 2013)
969	1026	Trough	Moisture, biomass/yield, starch	Hatfield <i>et al.</i> (2019); Mobasheri and Rahimzadegan (2012); Roberts <i>et al.</i> (2018); Serrano <i>et al.</i> (2002); Thenkabail <i>et al.</i> (2021)
998	190	Trough	Moisture, biomass/yield, protein, starch	Aneece and Thenkabail (2018); Mobasheri and Rahimzadegan (2012)
1099	87	Peak	Biomass/yield, LAI	Mariotto <i>et al.</i> (2013); Thenkabail <i>et al.</i> (2004)
1142	1273	Peak	Biomass/yield, water content, lignin	Clevers (2014); Mariotto <i>et al.</i> (2013); Mobasheri and Rahimzadegan (2012); Thenkabail <i>et al.</i> (2004)
1152	893	Trough	Biomass/yield	Mariotto <i>et al.</i> (2013)
1185	339	Trough	Biomass/yield, moisture	Mariotto <i>et al.</i> (2013); Roberts <i>et al.</i> (2018)
1218	234	Trough***	Moisture	Aneece and Thenkabail (2018); Hatfield <i>et al.</i> (2019); Roberts <i>et al.</i> (2018); Thenkabail <i>et al.</i> (2004)
1240	1142	Trough	Water sensitivity	Thenkabail <i>et al.</i> (2021)
1273	1103	Peak	Biomass/yield	Mariotto <i>et al.</i> (2013)
1459	1460	Peak	Moisture, lignin, nitrogen, classification, starch, sugar	Mobasheri and Rahimzadegan (2012); Roberts <i>et al.</i> (2018); Serrano <i>et al.</i> (2002); Singh <i>et al.</i> (2022); Thenkabail <i>et al.</i> (2021)
1470	865	Trough	Biomass/yield, moisture	Mariotto <i>et al.</i> (2013); Thenkabail <i>et al.</i> (2004)
1687	38	Peak*	Biomass/yield, lignin, starch, protein	Mariotto <i>et al.</i> (2013); Mobasheri and Rahimzadegan (2012); Serrano <i>et al.</i> (2002)
1993	1421	Peak	Biomass/yield, nitrogen	Mariotto <i>et al.</i> (2013); Singh <i>et al.</i> (2022)
2053	1440	Trough	Biomass/yield, proteins, lignin, cellulose, nitrogen	Mariotto <i>et al.</i> (2013); Mobasheri and Rahimzadegan (2012); Roberts <i>et al.</i> (2018); Thenkabail <i>et al.</i> (2004)
2061	1139	Peak	Moisture, nitrogen, protein	Aneece and Thenkabail (2018); Mobasheri and Rahimzadegan (2012); Serrano <i>et al.</i> (2002)
2207	432	Peak*	Lignin, cellulose, sugar, starch, protein	Aneece and Thenkabail (2018); Roberts <i>et al.</i> (2018); Thenkabail <i>et al.</i> (2014, 2013)
2321	1443	Trough	Biomass/yield, stress moisture, lignin, starch	Mariotto <i>et al.</i> (2013); Mobasheri and Rahimzadegan (2012); Thenkabail <i>et al.</i> (2004)
2357	1201	Trough	Cellulose, protein, nitrogen	Mobasheri and Rahimzadegan (2012); Thenkabail <i>et al.</i> (2021)
2400	1058	Peak	Cellulose, lignin, protein	Roberts <i>et al.</i> (2018)
2428	1368	Peak	Undetermined	This study
2449	1319	Trough	Undetermined	This study
2463	1106	Peak	Undetermined	This study

LAI = Leaf Area Index; LULC = Land Use/Land Cover; LUE = Light Use Efficiency.

*Local trough within a peak; **Frequency of 0 but included because important for subsequent analyses; ***Local peak within water absorption.

Table 8. Hyperspectral vegetation indices (HVI) sourced from literature, for which specific narrowband centers were selected from optimal hyperspectral narrowbands (OHNB) of PRecursores IperSpettrale della Missione Applicativa (PRISMA) from this study.

Index	References
Biomass, Vegetation Density, Vegetation Fraction, Leaf Area Index	
Normalized Difference Vegetation Index (NDVI), $NDVI = \frac{R_{834} - R_{670}}{R_{834} + R_{670}}$	Giovos <i>et al.</i> (2021); Kior <i>et al.</i> (2021); Segarra <i>et al.</i> (2020); Zhang <i>et al.</i> (2021b)
Green Normalized Difference Vegetation Index (GNDVI), $GNDVI = \frac{R_{781} - R_{555}}{R_{781} + R_{555}}$	Giovos <i>et al.</i> (2021); Kior <i>et al.</i> (2021); Poley and McDermid (2020); Zhang <i>et al.</i> (2021b)
Enhanced Vegetation Index (EVI), $EVI = 2.5 * \left(\frac{R_{781} - R_{670}}{R_{781} + (C1 * R_{670}) - (C2 * R_{442}) + L} \right)$	Kior <i>et al.</i> (2021); Poley and McDermid (2020); Roberts <i>et al.</i> (2018); Zhang <i>et al.</i> (2021b)
Soil-Adjusted Vegetation Index (SAVI), $SAVI = \frac{(R_{791} - R_{670}) * (1 + L)}{R_{791} + R_{670} + L}$	Hatfield <i>et al.</i> (2019); Kior <i>et al.</i> (2021); Roberts <i>et al.</i> (2018)
Atmospherically-Resistant Vegetation Index (ARVI), $ARVI = \frac{R_{781} - (R_{670} * R_{442})}{R_{781} + (R_{670} * R_{442})}$	Kior <i>et al.</i> (2021); Roberts <i>et al.</i> (2018)
Nitrogen Content	
Normalized Difference Nitrogen Index (NDNI), $NDNI = \frac{\log(1 / R_{1512}) - \log(1 / R_{1687})}{\log(1 / R_{1512}) + \log(1 / R_{1687})}$	Roberts <i>et al.</i> (2018); Serrano <i>et al.</i> (2002)
Chlorophyll Content	
Modified Chlorophyll Absorption in Reflectance Index (MCARI), $MCARI = [R_{719} - R_{670} - 0.2(R_{719} - R_{555})] * \left(\frac{R_{719}}{R_{670}} \right)$	Clevers (2014); Giovos <i>et al.</i> (2021); Kior <i>et al.</i> (2021); Poley and McDermid (2020); Roberts <i>et al.</i> (2018); Zhang <i>et al.</i> (2021b)
Triangular Greenness Index (TGI), $TGI = -0.5 * [228(R_{670} - R_{555}) - 115(R_{670} - R_{442})]$	Hunt <i>et al.</i> (2013); Segarra <i>et al.</i> (2020)
Triangular Vegetation Index (TVI), $TVI = 0.5 * [115(R_{750} - R_{555}) - 195(R_{670} - R_{555})]$	Hatfield <i>et al.</i> (2019); Hunt <i>et al.</i> (2013); Kior <i>et al.</i> (2021); Poley and McDermid (2020)
Gitelson's Chlorophyll Index 1, $Gitelson - chl1 = \left(\frac{1}{R_{555}} - \frac{1}{R_{781}} \right) * R_{781}$	Giovos <i>et al.</i> (2021); Gitelson <i>et al.</i> (2006); Kandalakis and Karantzalos (2016)
Normalized Pigment Chlorophyll Index (NPCI), $NPCI = \frac{R_{670} - R_{427}}{R_{670} + R_{427}}$	Hatfield <i>et al.</i> (2019); Kandalakis and Karantzalos (2016); Kior <i>et al.</i> (2021); Poley and McDermid (2020)
Carotenoid Content	
Gitelson's Carotenoid Index 1, $Gitelson - car1 = \left(\frac{1}{R_{515}} - \frac{1}{R_{555}} \right) * R_{781}$	Giovos <i>et al.</i> (2021); Gitelson <i>et al.</i> (2006); Kandalakis and Karantzalos (2016)
Blackburn's Carotenoid Index 2, $Blackburn - car2 = \frac{R_{802} - R_{471}}{R_{802} + R_{471}}$	Giovos <i>et al.</i> (2021); Gitelson <i>et al.</i> (2002); Kandalakis and Karantzalos (2016)
Anthocyanin Content	
Anthocyanin Reflectance Index 2 (ARI2), $ARI2 = R_{802} * \left(\frac{1}{R_{555}} - \frac{1}{R_{719}} \right)$	Gitelson <i>et al.</i> (2001); Kior <i>et al.</i> (2021); Roberts <i>et al.</i> (2018)
Anthocyanin Content Index (ACI), $ACI = \frac{R_{555}}{R_{781}}$	Giovos <i>et al.</i> (2021); Roberts <i>et al.</i> (2018)
Water Content	
Normalized Difference Water Index (NDWI), $NDWI = \frac{R_{866} - R_{1240}}{R_{866} + R_{1240}}$	Clevers (2014); Giovos <i>et al.</i> (2021); Kior <i>et al.</i> (2021)
Water Index (WI), $WI = \frac{R_{898}}{R_{969}}$	Clevers (2014); Giovos <i>et al.</i> (2021); Kior <i>et al.</i> (2021); Roberts <i>et al.</i> (2018)
Structural Content	
Cellulose Absorption Index (CAI), $CAI = 0.5(R_{2019} + R_{2207}) - R_{2111}$	Daughtry (2001); Roberts <i>et al.</i> (2018)
Normalized Difference Lignin Index (NDLI), $NDLI = \frac{\log(1 / R_{1756}) - \log(1 / R_{1687})}{\log(1 / R_{1756}) + \log(1 / R_{1687})}$	Roberts <i>et al.</i> (2018); Serrano <i>et al.</i> (2002)
Stress	
Moisture Stress Index (MSI), $MSI = \frac{R_{1687}}{R_{929}}$	Giovos <i>et al.</i> (2021); Kior <i>et al.</i> (2021); Roberts <i>et al.</i> (2018)
Carter Index 1, $Ctr1 = \frac{R_{695}}{R_{427}}$	Carter (1994); Giovos <i>et al.</i> (2021); Kandalakis and Karantzalos (2016); Kior <i>et al.</i> (2021)
Lichtenthaler Index 2, $Lic2 = \frac{R_{442}}{R_{695}}$	Kior <i>et al.</i> (2021); Lichtenthaler <i>et al.</i> (1996); Zarco-Tejada <i>et al.</i> (2005)
Photochemical Reflectance Index (PRI), $PRI = \frac{R_{531} - R_{571}}{R_{531} + R_{571}}$	Giovos <i>et al.</i> (2021); Hatfield <i>et al.</i> (2019); Kior <i>et al.</i> (2021); Roberts <i>et al.</i> (2018)
Shortwave Infrared Water Stress Index (SIWSI), $SIWSI = \frac{R_{866} - R_{1687}}{R_{866} + R_{1687}}$	Giovos <i>et al.</i> (2021); Hatfield <i>et al.</i> (2019)
Vogelmann Index 2, $Vog2 = \frac{R_{739} - R_{750}}{R_{719} + R_{729}}$	Giovos <i>et al.</i> (2021); Vogelmann <i>et al.</i> (1993); Zarco-Tejada <i>et al.</i> (2005)
Normalized Multi-Band Drought Index (NMDI), $NMDI = \frac{R_{866} - (R_{1687} - R_{2207})}{R_{866} + (R_{1687} - R_{2207})}$	Kior <i>et al.</i> (2021); Wang and Qu (2007)

agricultural crops (almonds, corn, cotton, grapes, pistachios, rice, and tomatoes). These spectral libraries were used to compare DESIS and PRISMA data characteristics. DESIS data, with narrower bands, had more spectral features (peaks and troughs) than did PRISMA data. However, given the lower classification accuracies using DESIS data, these spectral features may be more noise than information. This performance can be attributed to the issues of sensor SNR related to the very narrow spectral bandwidth of 2.55 nm in DESIS. It has been observed that the signal in the visible portion of the spectrum (400–700 nm) in DESIS is low and the noise in the 760–1000 nm range is high. There is also an issue of overcorrection in DESIS or a sensor-related issue where we have noticed a number of bands with zero reflectivity in the 400–700 nm range. Very narrow bands have high SNR when data are collected from the ground using a spectroradiometer. However, when collected from spaceborne sensors, SNR can be low for very narrow bands such as the 2.55 nm of DESIS relative to the slightly broader ≤ 12 nm of PRISMA. Field data are needed to determine optimal bandwidths. Thus, when conducting inter-sensor comparisons, differences in sensor characteristics (e.g., bandwidth) and in data preprocessing (e.g., atmospheric correction) need to be kept in mind.

DESIS and PRISMA spectral libraries were used to determine OHNB for each sensor, retaining 11–19% non-redundant hyperspectral data. This percentage of unique information retained is consistent with other hyperspectral literature (Anece and Thenkabail 2021; Mariotto *et al.* 2013; Marshall *et al.* 2016; Thenkabail *et al.* 2021). Some spectral features seen in DESIS and PRISMA data may be sensor or detector artifacts, or products of the atmospheric correction methods used. For example, the peak at 771 nm in PRISMA data may be influenced by correction of the oxygen absorption feature. The peaks observed in the NIR region, especially in the water absorption feature from 910 to 1000 nm, may be influenced by the low SNR in that spectral range. Determining the level of signal versus noise and artifacts will allow us to evaluate the extrapolability of these results in other areas and using other sensors.

Further, the selected features and corresponding OHNB fall in regions of the spectral profile correlated with plant characteristics as determined in agricultural remote sensing literature (Anece and Thenkabail 2018, 2021; Chen *et al.* 2020; Clevers 2014; Delalieux *et al.* 2007; Deng *et al.* 2020; Hatfield *et al.* 2019; Hennessy *et al.* 2020; Ma *et al.* 2019; Mariotto *et al.* 2013; Mobasheri and Rahimzadegan 2012; Mudereri *et al.* 2020; Ren *et al.* 2020; Roberts *et al.* 2018; Salem *et al.* 2017; Serrano *et al.* 2002; Singh *et al.* 2022; Thenkabail 2015; Thenkabail *et al.* 2021, 2014; Zhang *et al.* 2018). These OHNB were able to differentiate the seven crop types. The overall accuracies were higher for PRISMA (90%) than for DESIS (83%) in the 400 to 1000 nm range. Using the PRISMA OHNB from 400 to 1000 nm, we obtained producer's accuracies of 72 to 100% and user's accuracies of 80 to 100%. These accuracies were obtained using the support vector machine classification algorithm. Higher accuracies may be obtained using deep learning algorithms (Raczko and Zagajewski 2017). Bands beyond 1000 nm in PRISMA did not result in increased accuracies. However, these bands will likely improve results in studies pertaining to crop biophysical/biochemical properties.

Lastly, PRISMA narrowbands were used to adapt vegetation indices for estimation of various plant characteristics including pigment content, stress, biomass, and cellulose/lignin content (Table 8). For example, the Normalized Difference Vegetation Index (NDVI) has been used in many studies to estimate vegetation growth and health. However, it has issues of saturation in areas with high amounts of vegetation and can be influenced by soil and atmosphere (Roberts *et al.* 2018). The Green Normalized Difference Vegetation Index (GNDVI) is similar to NDVI, but more sensitive to chlorophyll content (Kior *et al.* 2021). The Soil-Adjusted Vegetation Index (SAVI) and the Atmospherically-Resistant Vegetation Index (ARVI) minimize influence from soil properties and atmospheric conditions respectively (Roberts *et al.* 2018). The Enhanced Vegetation Index (EVI) also includes corrections for differences in soil properties and atmospheric conditions and is less susceptible to problems of saturation (Roberts *et al.* 2018).

Many indices also exist for estimating nitrogen and pigment content. Nitrogen is used by plants for building pigments and proteins, influencing the spectral profile throughout the spectral range. The Normalized Difference Nitrogen Index (NDNI) compares the nitrogen absorbance around 1510 nm with the non-absorbing region around 1680 nm (Roberts *et al.* 2018). However, nitrogen estimation can be challenging because absorption features around 1500 and 2180 nm are masked by water absorption features in healthy plants (Clevers 2014).

Several chlorophyll indices use the chlorophyll absorption band around 670 nm and the green peak around 550 nm. For example, the Chlorophyll Absorption in Reflectance Index (CARI) compares the reflectance around 670 nm with reflectance in the red (R) region, around 700 nm. The modified CARI (MCARI) includes a ratio between the NIR and R regions to compensate for soil (Roberts *et al.* 2018). The Triangular Greenness Index (TGI) allows for estimation of chlorophyll without the need for a red-edge band; it instead uses reflectances around 670, 550, and 480 nm (Hunt *et al.* 2013). Similarly, the Triangular Vegetation Index (TVI) uses reflectances around 670, 550, and 750 nm to form a triangle to estimate chlorophyll and LAI (Hunt *et al.* 2013; Kior *et al.* 2021). The Normalized Pigment Chlorophyll Index (NPCI) estimates the ratio of total pigments to chlorophyll and can be used to assess plant stress (Penuelas *et al.* 1994). Carotenoids play a role in photosynthesis and the protection of chlorophyll from photooxidation (Gitelson *et al.* 2006; Roberts *et al.* 2018). Both chlorophylls and carotenoids influence spectral reflectances in the green region. Thus, bands to estimate concentrations of individual pigment types need to use bands that are influenced only by one pigment type, as done by Gitelson *et al.* (2006) and Blackburn (1998) to estimate carotenoid content. Carotenoids are most easily detected during plant senescence, when chlorophyll breaks down while carotenoids are still intact (Roberts *et al.* 2018). Similarly, anthocyanins also play a role during periods of stress, and are thought to reduce photoinhibition (Roberts *et al.* 2018). Leaves have a reddish color when high in anthocyanin content. The Anthocyanin Reflectance Index (ARI) takes the difference between the reciprocals of the green and red-edge reflectances. ARI-2 refines the estimation by adding a weighting through NIR reflectance (Roberts *et al.* 2018). The Anthocyanin Content Index uses the ratio between green and NIR reflectances to measure the drop in green leaf reflectance with increasing anthocyanin content (Roberts *et al.* 2018).

For estimating plant moisture/water content, the Normalized Difference Water Index (NDWI) compares reflectance values around 860 and 1240 nm to estimate plant moisture while minimizing atmospheric influences (Kior *et al.* 2021). The Water Index, also called the Water Band Index, compares reflectances at 900 and 970 nm to detect the amount of water absorption and estimate plant moisture (Roberts *et al.* 2018). To estimate cellulose content, the Cellulose Absorption Index (CAI) uses the cellulose absorption band around 2101 nm and surrounding bands outside of the absorption feature (Roberts *et al.* 2018). Similarly, the Normalized Difference Lignin Index (NDLI) compares reflectance at the lignin absorption band around 1754 nm with the non-absorbing region around 1680 nm (Roberts *et al.* 2018).

As plants face several stressors, there are many indices used to estimate plant stress. The Moisture Stress Index (MSI) compares reflectance at the water absorption band around 1650 nm with NIR reflectance (either around 830 nm or 927 nm) (Roberts *et al.* 2018). The Carter Index 1 (Ctri1) uses reflectances around 695 and 420 nm to estimate stress regardless of the stressor (Carter 1994). Similarly, the Lichtenthaler Index 2 (Lic2) uses reflectances around 695 and 440 nm to detect inhibition of photosynthesis and stress (Lichtenthaler *et al.* 1996). The Photochemical Reflectance Index measures the decrease in reflectance at 531 nm by comparing it with reflectance at 570 nm (Roberts *et al.* 2018). This decrease can be used to estimate plant stress or carotenoid content (Roberts *et al.* 2018). The Shortwave Infrared Water Stress Index (SIWSI) uses reflectances around 860 and 1650 nm to detect water stress (Hatfield *et al.* 2019). The Vogelmann Index 2 uses red edge bands to detect low chlorophyll levels and estimate stress (Giovos *et al.* 2021; Vogelmann *et al.* 1993). Finally, the Normalized

Multi-Band Drought Index (NMDI) uses the water absorption bands around 860, 1640, and 2130 nm (MODIS bands 2, 6, and 7, respectively) to estimate plant and soil moisture to assess drought stress (Wang and Qu 2007).

These existing vegetation indices were adapted to PRISMA data considering available bands, spectral features seen in the spectral libraries, and PRISMA OHNB. The bands included in these indices sometimes differ from those in literature because of differences in bandwidths across sensors. For example, the NMDI was built using available MODIS bands, but may benefit from using narrower PRISMA bands like those recommended here. The recommended bands are also sometimes adjusted to take into account PRISMA spectral features. For example, 550 nm is often used to represent the green band. Here, we found the green peak most often occurred at 555 nm, and thus recommended this to be used (Table 8). Index parameters also needed to be adjusted when adjusting bands in certain indices. For example, the values of 228 and 115 in the TGI represent differences between band values (i.e., $670 - 442 = 228$ and $670 - 555 = 115$). A similar adjustment was made to the TVI. In cases where very broad spectral regions were indicated in the equations (e.g., NIR/R), we used literature review and PRISMA features/OHNB to recommend narrowbands. Further exploration, especially in conjunction with field measurements, will help further refine these recommendations.

In addition to adapting existing vegetation indices, we suggested HTBVI that may be used to estimate various plant biophysical and biochemical characteristics using PRISMA narrowbands (Table 9). Using the existing knowledge-base (for example Thenkabail *et al.* (2018a, 2018b, 2018c, 2018d)), we have attempted to define spectral bands of importance considering various peaks and troughs throughout the electromagnetic spectrum. These important peaks and troughs were determined based on their consistent occurrence and patterns observed across crop types and dates using large sample sizes and literature review. Regardless, further research, alongside field-observed data, will allow each of these HTBVI to be specifically linked to a particular biochemical or biophysical characteristic. These suggested indices are meant to serve as a pathway for further research.

The DESIS and PRISMA spectral libraries developed here alongside others in the Global Hyperspectral Imaging Spectral-libraries of Agricultural crops (GHISA) project (Thenkabail *et al.* 2019), will facilitate development and automated deployment of crop type machine-deep learning classification algorithms. In addition, such inter-sensor comparisons at overlapping study areas and time-periods are crucial for future workflows taking advantage of these and upcoming hyperspectral sensors for crop type mapping and crop productivity estimations.

Of course, there is much work to be done. Our goal for this study was to assess any advantages that would be provided by the narrower DESIS bands; however, future work could include comparing classification accuracies using the various binned DESIS products. It also includes testing of the adapted VI and suggested HTBVI with ground measurements of plant characteristics. Additionally, small spectral features from DESIS data need to be examined alongside field data to determine whether they encompass noise or information. These sensor comparisons could be furthered by adding future sensors such as the recently launched German EnMAP and upcoming US NASA SBG sensors. The data from these future sensors will also increase image availability for time-series classification analyses.

Conclusions

DESIS and PRISMA new generation spaceborne hyperspectral sensors were used to develop spectral libraries of seven agricultural crops (almonds, corn, cotton, grapes, pistachios, rice, and tomatoes) in the Central Valley of California, USA for the growing season of 2020. Inter-sensor comparisons of these two hyperspectral sensors indicated high correlations with R^2 values of 0.90–0.95. The study established 26 DESIS optimal hyperspectral narrow bands (OHNB) (11% of the 235 DESIS HNB from 400 to 1000 nm) and 45 PRISMA OHNB (19% of the

238 PRISMA HNB from 400 to 2500 nm) for the study of agricultural crops. The rest (89% of DESIS and 81% of PRISMA) of the bands were found to be redundant. The seven agricultural crops were classified with overall accuracies of 83–90% using these OHNB. Producer's accuracies of individual crop types for PRISMA ranged from 72 to 100% whereas those for DESIS ranged from 63 to 100%. User's accuracies of individual crop types for PRISMA ranged from 80 to 100% while those from DESIS ranged from 67 to 100%. Overall, PRISMA yielded substantially higher classification accuracies as a result of higher signal to noise ratio. HNB have shown great advances in the study of agricultural crops and vegetation. However, this study indicates there is an optimal bandwidth for spaceborne sensors below which SNR ratio decreases. Here, the ≤ 12 nm bandwidth of PRISMA provided more signal and less noise than the 2.55 nm bandwidth of DESIS. Finally, based on literature review and these OHNB, we developed hyperspectral two-band vegetation indices and adapted existing vegetation indices for PRISMA bands to estimate plant pigment content, plant stress, wet and dry biomass, plant water/moisture content, and cellulose/lignin content.

Acknowledgments

This research was supported by the National Land Imaging (NLI) Program, Land Change Science (LCS) program, and the Core Science Systems (CSS) of the United States Geological Survey (USGS). The research was conducted in the science facilities of the USGS Western Geographic Science Center (WGSC). Any use of trade, firm, or product names is for descriptive purposes only and does not imply endorsement by the US Government.

Data used in this study are available online through the ScienceBase Catalog (Aneece and Thenkabail 2022).

References

- Ali, M. and D. Clausi. (2001). Using the canny edge detector for feature extraction and enhancement of remote sensing images. Pages 2298–2300 in *Proceedings IEEE 2001 International Geoscience and Remote Sensing Symposium*, vol. 5, held in Sydney, Australia, 9–13 July 2001.
- Alonso, K., M. Bachmann, K. Burch, E. Carmona, D. Cerra, R. de los Reyes, D. Dietrich, U. Heiden, A. Holderlin, J. Ickes, U. Knodt, D. Krutz, H. Lester, R. Muller, M. Pagnutti, P. Reinartz, R. Richter, R. Ryan, I. Sebastian and M. Tegler. 2019. Data products, quality and validation of the DLR Earth Sensing Imaging Spectrometer (DESIS). *Sensors* 19(4471):1–44.
- Aneece, I. and P. Thenkabail. 2018. Accuracies achieved in classifying five leading world crop types and their growth stages using optimal Earth Observing-1 Hyperion hyperspectral narrow-bands on Google Earth Engine. *Remote Sensing* 10:29.
- Aneece, I. and P. Thenkabail. 2021. Classifying crop types using two generations of hyper-spectral sensors (Hyperion and DESIS) with machine learning on the cloud. *Remote Sensing* 13(4704):1–24.
- Aneece, I. and P. S. Thenkabail. 2022. *DESIS and PRISMA Spectral Library of Agricultural Crops in California's Central Valley in the 2020 Growing Season*. U.S. Geological Survey Data Release. <https://doi.org/10.5066/P98LO5D4>.
- Aphalo, P. 2020. *Learn R: As a Language. The R Series*. Boca Raton and London: Chapman and Hall/CRC Press.
- Bannari, A., K. Staenz, C. Champagne and K. Khurshid. 2015. Spatial variability mapping of crop residue using Hyperion (EO-1) hyperspectral data. *Remote Sensing* 7:8107–8127.
- Berk, A., G. Anderson, P. Acharya and E. Shettle. 2008. *MODTRAN 5.2.0.0 User's Manual*. Technical report.
- Bhojaraja, B., A. Shetty, M. K. Nagaraj and P. Manju. 2015. Age-based classification of areca nut crops: A case study of Channagiri, Karnataka, India. *Geocarto International* 1–11.
- Blackburn, G. 1998. Quantifying chlorophylls and carotenoids at leaf and canopy scales: An evaluation of some hyperspectral approaches. *Remote Sensing of Environment* 66(3):273–285.
- Boryan, C. and Z. Yang. 2021. Integration of the cropland data layer based automatic stratification method into the traditional area frame construction process. *Survey Research Methods* 11(3):289–306.

- Bresciani, M., C. Giardino, A. Fabbretto, A. Pellegrino, S. Mangano, G. Free and M. Pinardi. 2022. Application of new hyperspectral sensors in the remote sensing of aquatic ecosystem health: Exploiting PRISMA and DESIS for four Italian lakes. *Resources* 11(8):1–17.
- Breunig, F., L. Galvao, A. Formaggio and J. Epiphany. 2011. Classification of soybean varieties using different techniques: Case study with Hyperion and sensor spectral resolution simulations. *Journal of Applied Remote Sensing* 5:053533-1-053533-15.
- California Grown. 2022. *California Grown: What's in Season in California?* <<https://californiagrown.org/blog/whats-in-season-in-california>> Accessed 9 June 2022.
- Carter, G. 1994. Ratios of leaf reflectances in narrow wavebands as indicators of plant stress. *International Journal of Remote Sensing* 15:697–703.
- Chen, Z., K. Jia, C. Xiao, D. Wei, X. Zhao, J. Lan, X. Wei, Y. Yao, B. Wang, Y. Sun and L. Wang. 2020. Leaf area index estimation algorithm for GF-5 hyperspectral data based on different feature selection and machine learning methods. *Remote Sensing* 12(2110):1–23.
- Clevers, J. 2014. Chapter 22: Beyond NDVI: Extraction of biophysical variables from remote sensing imagery. In *Remote Sensing and Digital Image Processing*, volume Land Use and Land Cover Mapping in Europe: Practices and Trends. New York: Springer, pp. 363–381.
- Cogliati, S., F. Sarti, L. Chiarantini, M. Cosi, R. Lorusso, E. Lopinto, F. Miglietta, L. Genesio, L. Guanter, A. Damm, S. Pérez-López, D. Scheffler, G. Tagliabue, C. Panigada, U. Rascher, T. Dowling, C. Giardino and R. Colombo. 2021. The PRISMA imaging spectroscopy mission: Overview and first performance analysis. *Remote Sensing of Environment* 262:112499.
- CUESA (Center for Urban Education about Sustainable Agriculture). 2022. Center for Urban Education about Sustainable Agriculture—Seasonality Chart: Fruit and Nuts. <<https://cuesa.org/eat-seasonally/charts/fruit>> Accessed 09 June 2022.
- Daughtry, C. 2001. Discriminating crop residues from soil by shortwave infrared reflectance. *Agronomy Journal* 93:125–131.
- Delalieux, S., J. Aardt, W. Keulemans, E. Schrevels and P. Coppin. 2007. Detection of biotic stress (*Venturia inaequalis*) in apple trees using hyperspectral data: Non-parametric statistical approaches and physiological implications. *European Journal of Agronomy* 27:130–143.
- Deng, X., Z. Zhu, J. Yang, Z. Zheng, Z. Huang, X. Yin, S. Wei and Y. Lan. 2020. Detection of citrus Huanglongbing based on multi-input neural network model of UAV hyperspectral remote sensing. *Remote Sensing* 12(2678):1–20.
- EnMAP. 2022. Welcome to EnMAP: The German Spaceborne Imaging Spectrometer Mission. <<https://www.enmap.org/>> Accessed 17 June 2022.
- ESRI (Environmental Systems Research Institute). 2022. *ArcGIS Desktop: Release 10.8.1*. Redlands, CA: Environmental Systems Research Institute.
- Feng, L., Z. Zhang, Y. Ma, Q. Du, P. Williams, J. Drewry and B. Luck. 2020. Alfalfa yield prediction using UAV-based hyperspectral imagery and ensemble learning. *Remote Sensing* 12(2028):1–24.
- German Aerospace Center (formerly DLR) and Teledyne Brown. 2022. TCloud: Teledyne Technologies. <<http://tcloudhost.com/>> Last accessed [01/15/2022]. Last accessed [06/09/2022].
- Giovos, R., D. Tassopoulos, D. Kalivas, N. Lougkos and A. Priovolou. 2021. Remote sensing vegetation indices in viticulture: A critical review. *Agriculture* 11(457):1–20.
- Gitelson, A., G. Keydan and M. Merzlyak. 2006. Three-band model for noninvasive estimation of chlorophyll, carotenoids, and anthocyanin content in higher plant leaves. *Geophysical Research Letters* 33:38–45.
- Gitelson, A., M. Merzlyak and O. Chivkunova. 2001. Optical properties and nondestructive estimation of anthocyanin content in plant leaves. *Photochemistry and Photobiology* 71:38–45.
- Gitelson, A., Y. Zur, O. Chivkunova and M. Merzlyak. 2002. Assessing carotenoid content in plant leaves with reflectance spectroscopy. *Photochemistry and Photobiology* 75(3):272–281.
- Gopinath, G., N. Sasidharan and U. Surendran. 2020. Land use classification of hyperspectral data by spectral angle mapper and support vector machine in humid tropical region of India. *Earth Science Information* 13:633–640.
- Hank, T., K. Berger, M. Woher, M. Danner and W. Mauser. 2021. Introducing the potential of the EnMAP-box for agricultural applications using DESIS and PRISMA data. Pages 467–470 in *Proceedings 2021 IEEE International Geoscience and Remote Sensing Symposium*, held in Brussels, Belgium, 11–16 July 2021.
- Hao, P., L. Wang, Y. Zhan, C. Wang, Z. Niu and M. Wu. 2016. Crop classification using crop knowledge of the previous-year: Case study in Southwest Kansas, USA. *European Journal of Remote Sensing* 49(1):1061–1077.
- Hatfield, J., J. Prueger, T. Sauer, C. Dold, P. O'Brien and K. Wacha. 2019. Applications of vegetative indices from remote sensing to agriculture: Past and future. *Inventions* 4(71):1–17.
- Heiden, U., M. Bachmann, K. Alonso, E. Carmona, D. Cerra, D. Dietrich, M. Langheinrich, R. de los Reyes, R. Mueller, N. Pinnel and V. Ziel. 2019. DESIS imaging spectrometer data access and synergistic use with other ISS earth observing instruments. In *Proceedings Workshop on International Cooperation in Spaceborne Imaging Spectroscopy*, held in Frascati, Italy, 9–11 July 2019, <https://elib.dlr.de/129175/>.
- Hennessy, A., K. Clarke and M. Lewis. 2020. Hyperspectral classification of plants: A review of waveband selection generalisability. *Remote Sensing* 12(113):1–27.
- Houborg, R., M. McCabe, Y. Angel and E. Middleton. 2016. Detection of chlorophyll and leaf area index dynamics from sub-weekly hyperspectral imagery. In *Remote Sensing for Agriculture, Ecosystems, and Hydrology XVIII*, volume 9998, pp. 999812–1–999812–11. <https://doi.org/10.1117/12.2241345>.
- Hunt, E., P. Doraiswamy, J. McMurtry, C. Daughtry, E. Perry and A. Bakhyt. 2013. A visible band index for remote sensing leaf chlorophyll content at the canopy scale. *Publications from USDA-ARS / UNL Faculty*, pp. 1–13.
- Italian Space Agency (ASI). 2022. ASI data portal, PRISMA Catalogue Client. <<http://asi.it>> Accessed 09 June 2022.
- Kandylakis, Z. and K. Karantzalos. 2016. Precision viticulture from multitemporal, multispectral very high resolution satellite data. Pages 919–925 in *Proceedings of the XXII ISPRS Congress*, volume XLI-B8, held in Prague, Czech Republic.
- Kennedy, B., D. King and J. Duffe. 2020. Comparison of empirical and physical modelling for estimation of biochemical and biophysical vegetation properties: Field scale analysis across an Arctic bioclimatic gradient. *Remote Sensing* 12:1–41.
- Kior, A., V. Sukhov and E. Sukhova. 2021. Application of reflectance indices for remote sensing of plants and revealing actions of stressors. *Photonics* 8(582):1–27.
- Krutz, D., R. Muller, U. Knodt, B. Gunther, I. Walter, I. Sebastian, T. Sauerlich, R. Reulke, E. Carmona, A. Eckardt, H. Venus, C. Fischer, B. Zender, S. Arloth, M. Lieder, M. Neidhardt, U. Grote, F. Schrandt, S. Gelmi and A. Wojtkowiak. 2019. The instrument design of the DLR Earth Sensing Imaging Spectrometer (DESI). *Sensors* 19(1622):1–16.
- Kutser, T., B. Paavel, C. Verpoorter, M. Ligi, T. Soomets, K. Toming and G. Casal. 2016. Remote sensing of black lakes and using 810 nm reflectance peak for retrieving water quality parameters of optically complex waters. *Remote Sensing* 8(6). <https://doi.org/10.3390/rs8060497>.
- Labate, D., M. Ceccherini, A. Cisbani, V. De Cosmo, C. Galeazzi, L. Giunti, M. Melozzi, S. Pieraccini and M. Stagl. 2009. The PRISMA payload optomechanical design, a high performance instrument for a new hyperspectral mission. *Acta Astronautica* 65:1429–1436.
- Lamparelli, R., J. Johann, E. Dos Santos, J. Esquerdo and J. Rocha. 2012. Use of data mining and spectral profiles to differentiate condition after harvest of coffee plants. *Engenharia Agricultura Jaboticabal* 32(1):184–196.
- Lark, T., I. Schelly and H. Gibbs. 2021. Accuracy, bias, and improvements in mapping crops and cropland across the United States using the USDA Cropland Data Layer. *Remote Sensing* 13(968):1–29.
- Lichtenthaler, H., M. Lang, M. Sowinska, F. Heisel and J. Miehe. 1996. Detection of vegetation stress via a new high resolution fluorescence imaging system. *Journal of Plant Physiology* 148:599–612.
- Lin, Z. and L. Yan. 2016. A support vector machine classifier based on a new kernel function model for hyperspectral data. *GIScience and Remote Sensing* 53(1):85–101.
- Loizzo, R., C. Ananasso, R. Guarini, E. Lopinto, L. Candela and A. Pisani. 2016. The PRISMA hyperspectral mission. In *Proceedings Workshop on Living Planet Symposium*, held in Prague, Czech Republic, 9–13 May 2019. <<https://lps16.esa.int/>>.
- Lu, B., P. Dao, J. Liu, Y. He and J. Shang. 2020. Recent advances of hyperspectral imaging technology and applications in agriculture. *Remote Sensing* 12:1–44.

- Ma, H., K. Zhao, X. Jin, J. Ji, Z. Qiu and S. Gao. 2019. Spectral difference analysis and identification of different maturity blueberry fruit based on hyperspectral imaging using spectral index. *International Journal of Agriculture and Biological Engineering* 134(3):134–140.
- Mariotto, I., P. Thenkabail, A. Huete, T. Slonecker and A. Platonov. 2013. Hyperspectral versus multispectral crop-productivity modeling and type discrimination for the HypSIRI mission. *Remote Sensing of Environment* 139:291–305.
- Marshall, M. and P. Thenkabail. 2015. Advantage of hyperspectral EO-1 Hyperion over multi-spectral IKONOS, GeoEye-1, WorldView-2, Landsat ETM+, and MODIS vegetation indices in crop biomass estimation. *ISPRS Journal of Photogrammetry and Remote Sensing* 108:205–218.
- Marshall, M., P. Thenkabail, T. Biggs and K. Post. 2016. Hyperspectral narrowband and multispectral broadband indices for remote sensing of crop evapotranspiration and its components (transpiration and soil evaporation). *Agricultural and Forest Meteorology* 218–219:122–134.
- Mobasheri, M. and M. Rahimzadegan. 2012. Introduction to protein absorption lines index for relative assessment of green leaves protein content using EO-1 Hyperion datasets. *Journal of Agricultural Science and Technology* 14:135–147.
- Moharana, S. and S. Dutta. 2016. Spatial variability of chlorophyll and nitrogen content of rice from hyperspectral imagery. *ISPRS Journal of Photogrammetry and Remote Sensing* 122:17–29.
- Mudereri, B., T. Dube, S. Niassy, E. Kimathi, T. Landmann, Z. Khan and E. Abdel-Rahman. 2020. Is it possible to discern Striga weed (*Striga hermonthica*) infestation levels in maize agro-ecological systems using in-situ spectroscopy? *International Journal of Applied Earth Observation and Geoinformation* 85(102008):1–14.
- Nigam, R., R. Tripathy, S. Dutta, N. Bhagia, R. Nagori, K. Chandrasekar, R. Kot, B. Bhattacharya and S. Ustin. 2019. Crop type discrimination and health assessment using hyperspectral imaging. *Current Science* 116(7):1108–1123.
- Oki, K., L. Shan, T. Saruwatari, T. Suham and K. Omasa. 2006. Evaluation of supervised classification algorithms for identifying crops using airborne hyperspectral data. *International Journal of Remote Sensing* 27(10):1993–2002.
- Pan, Z., J. Huang and F. Wang. 2013. Multi range spectral feature fitting for hyperspectral imagery in extracting oilseed rape planting area. *International Journal of Applied Earth Observation and Geoinformation* 25:21–29.
- Penuelas, J., J. Gamon, A. Fredeen, J. Merino and C. Field. 1994. Reflectance indices associated with physiological changes in nitrogen- and water-limited sunflower leaves. *Remote Sensing of Environment* 48(2):135–146.
- Pepe, M., L. Pompilio, B. Gioli, L. Busetto and M. Boschetti. 2020. Detection and Classification of Non-Photosynthetic Vegetation from PRISMA Hyperspectral Data in Croplands. *Remote Sensing* 12(23).
- Peschel, T., M. Beier, C. Damm, J. Hartung, R. Jende, S. Muller, M. Rohde, A. Gebhardt, S. Risse, I. Walter, I. Sebastia, and D. Krutz. 2018. Integration and testing of an imaging spectrometer for earth observation. Page 7 in *Proceedings International Conference on Space Optics*, held in Chania, Greece, 12 July 2019.
- Pignatti, S., N. Acito, U. Amato, R. Casa, F. Castaldi, R. Coluzzi, R. De Bonis, M. Diani, V. Imbrenda, G. Laneve, S. Matteoli, A. Palombo, S. Pascucci, F. Santini, T. Simoniello, C. Ananasso, G. Corsini and V. Cuomo. 2015. Environmental products overview of the Italian hyperspectral PRISMA mission: The SAP4PRISMA project. Page 5 in *Proceedings IEEE International Geoscience and Remote Sensing Symposium*, held in Milan, Italy. <https://doi.org/10.1109/IGARSS.2015.7326701>.
- Pignatti, S., A. Palombo, S. Pascucci, F. Romano, F. Santini, T. Simoniello, U. Amato, V. Cuomo, N. Acito, M. Diani, S. Matteoli, G. Corsini, R. Casa, R. De Bonis, G. Laneve and C. Ananasso. 2013. The PRISMA hyperspectral mission: Science, activities and opportunities for agriculture and land monitoring. Page 5 in *Proceedings IEEE International Geoscience and Remote Sensing Symposium*, held in Melbourne, Australia. <https://doi.org/10.1109/IGARSS.2013.6723850>.
- Poley, L. and G. McDermid. 2020. A systematic review of the factors influencing the estimation of vegetation aboveground biomass using unmanned aerial systems. *Remote Sensing* 12(1052):1–46.
- Praveen, Y., A. Kiranmai, K. Nikitha and V. Devi. 2016. Hyperspectral sensor data fusion at decision level using support vector machine. *International Journal of Research in Engineering and Technology* 5(12):14–18.
- Puletti, N., N. Camarretta and P. Corona. 2016. Evaluating EO-1 Hyperion capability for mapping conifer and broadleaved forests. *European Journal of Remote Sensing* 49(1):157–169.
- R Core Team. 2018. *R: A Language and Environment for Statistical Computing*. Vienna, Austria: R Foundation for Statistical Computing.
- Raczko, E. and B. Zagajewski. 2017. Comparison of support vector machine, random forest and neural network classifiers for tree species classification on airborne hyperspectral apex images. *European Journal of Remote Sensing* 50(1):144–154.
- Ren, J., Wang, R., Liu, G., Feng, R., Wang, Y., and Wu, W. (2020). Partitioned relief-F method for dimensionality reduction of hyperspectral images. *Remote Sensing*, 12(1104):1–21.
- Roberts, D., K. Roth, E. Wetherley, S. Meerdink and R. Perroy. 2018. Hyperspectral vegetation indices. In *Hyperspectral Remote Sensing of Vegetation*, Vol. II: Hyperspectral Indices and Image Classifications for Agriculture and Vegetation, 1–24. Boca Raton: Taylor and Francis Inc. CRC Press.
- Rodriguez-Galiano, V., M. Sanchez-Castillo, M. Chica-Olma and M. Chica-Rivas. 2015. Machine learning predictive models for mineral prospectivity: An evaluation of neural networks, random forest, regression trees and support vector machines. *Ore Geology Reviews* 71:804–818.
- Sacks, W., D. Deryng, J. Foley and N. Ramankutty. 2010. Crop planting dates: An analysis of global patterns. *Global Ecology and Biogeography* 19:607–620.
- Sahadevan, A. 2021. Extraction of spatial-spectral homogeneous patches and fractional abundances for field-scale agriculture monitoring using airborne hyperspectral images. *Computers and Electronics in Agriculture* 188(106325):1–11.
- Salas, E. and S. Subburayalu. 2019. Modified shape index for object-based random forest image classification of agricultural systems using airborne hyperspectral datasets. *PLoS ONE* 14(3):1–22.
- Salas, E., S. Subburayalu, B. Slater, K. Zhao, B. Bhattacharya, R. Tripathy, A. Das, R. Nigam, R. Dave and P. Parekh. 2020. Mapping crop types in fragmented arable landscapes using AVIRIS-NG imagery and limited field data. *International Journal of Image and Data Fusion* 11(1):33–56.
- Salem, S., H. Higa, H. Kim, H. Kobayashi, K. Oki and T. Oki. 2017. Assessment of chlorophyll-a algorithms considering different trophic statuses and optimal bands. *Sensors* 17(1746):1–24.
- Surface Biology and Geology (SBG). 2022. Jet Propulsion Laboratory California Institute of Technology: Surface Biology and Geology. <<https://sbg.jpl.nasa.gov/>>. Accessed 17 June 2022.
- Segarra, J., M. Buchailot, J. Araus and S. Kefauver. 2020. Remote sensing for precision agriculture: Sentinel-2 improved features and applications. *Agronomy* 10(641):1–18.
- Serrano, L., J. Penuelas and S. Ustin. 2002. Remote sensing of nitrogen and lignin in Mediterranean vegetation from AVIRIS data: Decomposing biochemical from structural signals. *Remote Sensing of Environment* 81:355–364.
- Singh, L., O. Mutanga, P. Mafongoya, K. Peerbhay and J. Crous. 2022. Hyperspectral remote sensing for foliar nutrient detection in forestry: A near-infrared perspective. *Remote Sensing Applications: Society and Environment* 25:1–13.
- Sonmez, N. and B. Slater. 2016. Measuring intensity of tillage and plant residue cover using remote sensing. *European Journal of Remote Sensing* 49(1):121–135.
- Thenkabail, P. 2015. Hyperspectral remote sensing for terrestrial applications. In *Remote Sensing Handbook*, Vol. II: Land Resources: Monitoring, Modeling, and Mapping: Advances over Last 50 Years and a Vision for the Future. New York: Taylor and Francis Inc., CRC Press.
- Thenkabail, P., I. Anece, P. Teluguntla and A. Oliphant. 2021. Hyperspectral narrowband data propel gigantic leap in the earth remote sensing, highlight article. *Photogrammetric Engineering and Remote Sensing* 87(7):461–467.
- Thenkabail, P., I. Anece, P. Teluguntla, A. Oliphant, D. Foley and D. Williamson. 2019. Global Hyperspectral Imaging Spectroscopy of Agricultural-Crops & Vegetation (GHISA). <usgs.gov>
- Thenkabail, P., E. Enclona, M. Ashton, C. Legg and M. De Dieu. 2004. Hyperion, IKONOS, ALI, and ETM+ sensors in the study of African rainforests. *Remote Sensing of Environment* 90:23–43.

- Thenkabail, P., M. Gumma, P. Teluguntla and I. Mohammed. 2014. Hyperspectral remote sensing of vegetation and agricultural crops. *Photogrammetric Engineering and Remote Sensing* 80(4):697–709.
- Thenkabail, P., G. Lyon and A. Huete. 2018a. Hyperspectral remote sensing of vegetation. In *Volume I: Fundamentals, Sensor Systems, Spectral Libraries, and Data Mining for Vegetation*, 449. New York: Taylor and Francis Inc., CRC Press.
- Thenkabail, P., G. Lyon and A. Huete. 2018b. Hyperspectral remote sensing of vegetation. In *Volume II: Hyperspectral Indices and Image Classifications for Agriculture and Vegetation*, 296. New York: Taylor and Francis Inc., CRC Press.
- Thenkabail, P., G. Lyon and A. Huete. 2018c. Hyperspectral remote sensing of vegetation. In *Volume III: Biophysical and Biochemical Characterization and Plant Species Studies*, 348. New York: Taylor and Francis Inc., CRC Press.
- Thenkabail, P., G. Lyon and A. Huete. 2018d. Hyperspectral remote sensing of vegetation. In *Volume IV: Advanced Applications in Remote Sensing of Agricultural Crops and Natural Vegetation*, 386. New York: Taylor and Francis Inc., CRC Press.
- Thenkabail, P., I. Mariotto, M. Gumma, E. Middleton, D. Landis and K. Huemmrich. 2013. Selection of hyperspectral narrowbands (HNBS) and composition of hyperspectral two band vegetation indices (HVIs) for biophysical characterization and discrimination of crop types using field reflectance and Hyperion/EO-1 data. *IEEE Journal of Selected Topics in Applied Earth Observations and Remote Sensing* 6(2):427–439.
- Tripathi, P. and R. Garg. 2021. Feature extraction of DESIS and PRISMA hyperspectral remote sensing datasets for geological applications. Pages 169–173 in *Proceedings ASPRS 2021 Annual Conference*. <https://doi.org/10.5194/isprs-archives-XLIV-M-3-2021-169-2021>.
- United States Department of Agriculture National Agricultural Statistics Service (USDA NASS). 2022. 2020 California Cropland Data Layer: NASS/USDA Metadata. <<https://www.nass.usda.gov/>>. Accessed 09 June 2022.
- United States Department of Agriculture (USDA) National Agricultural Statistics Service Cropland Data Layer. 2022. Published crop-specific data layer. <<https://nassgeodata.gmu.edu/CropScape/>>. Accessed 09 June 2022.
- Vali, A., S. Comai and M. Matteucci. 2020. Deep learning for land use and land cover classification based on hyperspectral and multispectral Earth observation data: A review. *Remote Sensing* 12:1–31.
- Vogelmann, J., B. Rock and D. Moss. 1993. Red edge spectral measurements from sugar maple leaves. *International Journal of Remote Sensing* 14(8):1563–1575.
- Wang, L. and J. Qu. 2007. NMDI: A normalized multi-band drought index for monitoring soil and vegetation moisture with satellite remote sensing. *Geophysical Research Letters* 34:1–6.
- Wickham, H. 2016. *Ggplot2: Elegant Graphics for Data Analysis* 2d ed. New York: Springer International Publishing.
- Yang, S., L. Hu, H. Wu, H. Ren, H. Qiao, P. Li and W. Fan. 2021. Integration of crop growth model and random forest for winter wheat yield estimation from UAV hyperspectral imagery. *IEEE Journal of Selected Topics in Applied Earth Observations and Remote Sensing* 14:6253–6269.
- Zarco-Tejada, P., A. Berjon, R. Lopez-Lozano, J. Miller, P. Martin, V. Cachorro, M. Gonzalez and A. de Frutos. 2005. Assessing vineyard condition with hyperspectral indices: Leaf and canopy reflectance simulation in a row-structured discontinuous canopy. *Remote Sensing of Environment* 99:271–287.
- Zarco-Tejada, P., J. Pushnik, S. Dobrowski and S. Ustin. 2003. Steady-state chlorophyll a fluorescence detection from canopy derivative reflectance and double-peak red-edge effects. *Remote Sensing of Environment* 84(2):283–294.
- Zhang, C., L. Di, P. Hao, Z. Yang, L. Lin, H. Zhao and L. Guo. 2021a. Rapid in-season mapping of corn and soybeans using machine-learned trusted pixels from Cropland Data Layer. *International Journal of Applied Earth Observation and Geoinformation* 102:1–14.
- Zhang, W., X. Li and L. Zhao. 2018. Band priority index: A feature selection framework for hyperspectral imagery. *Remote Sensing* 10(1095):1–19.
- Zhang, Y., C. Xia, X. Zhang, X. Cheng, G. Feng, Y. Wang and Q. Gao. 2021b. Estimating the maize biomass by crop height and narrowband vegetation indices derived from UAV-based hyperspectral images. *Ecological Indicators* 129:1–12.
- Zhong, L., P. Gong and G. Biging. 2014. Efficient corn and soybean mapping with temporal extendability: A multi-year experiment using Landsat imagery. *Remote Sensing of Environment* 140:1–13.